Cell Metabolic Alterations due to Mcph1 Mutation in Microcephaly

Nathalie Journiac, Javier Gilabert-Juan, Sara Cipriani, Paule Benit, Xiaoqian Liu, Sandrine Jacquier, Valérie Faivre, Andrée Delahaye-Duriez, Zsolt Csaba, Tristan Hourcade, et al.

Cell metabolic alterations due to Mcph1 mutation in microcephaly

Nathalie Journiac[1 # *], Javier Gilabert-Juan[1° *], Sara Cipriani[1§], Paule Benit[1], Xiaoqian Liu[2], Sandrine Jacquier[1], Valérie Faivre[1], Andrée Delahaye-Duriez[1,3], Zsolt Csaba[1], Tristan Hourcade[1], Eliza Melinte[1], Sophie Lebon[1], Céline Violle-Poirsier[4], Jean-François Oury[5], Homa Adle-Biassette[1,6], Zhao-Qi Wang[2,7], Shyamala Mani[1,8], Pierre Rustin[1], Pierre Gressens[1,9&] and Jeannette Nardelli[1&]

[1] PROTECT Inserm UMR 1141, Université Paris Diderot, Sorbonne Paris Cité, Paris, France

[2] Leibniz Institute on Aging – Fritz Lipmann Institute (FLI), Jena, Germany

[3] Service d'Histologie, Embryologie, et Cytogénétique, Hôpital Jean Verdier, Saint Denis, AP-HP, Université Paris 13, Sorbonne Paris Cité, Bobigny, France

[4] Service de Génétique et Biologie de la Reproduction, CHU Reims, France

[5] Service de Gynécologie-Obstétrique, Hôpital Robert Debré, AP-HP, Paris, France.

[6] Service d'Anatomie et de Cytologie Pathologiques, Hôpital Lariboisière, AP-HP, Paris, France

[7] Faculty of Biology and Pharmacy, Friedrich-Schiller University of Jena, Jena, Germany

[8] Curadev Pharma Pvt. Ltd., NOIDA, India

[9] Centre for the Developing Brain, Department of Perinatal Imaging and Health, Division of Imaging Sciences and Biochemical Engineering, King's College London, St. Thomas' Hospital, London

[#] Present address: Univ. Lille, Inserm, CHU Lille, U1172 - LilNCog - Lille Neuroscience & Cognition, F-59000 Lille, France

[§] Present address: Institute of Cardiometabolism And Nutrition (ICAN), IE3M, Paris, France.

[°] Present address: CNRS/UMR7241-Inserm U1050, Collège de France, Paris, France.

[*] These authors participated equally to this work

[&] Corresponding authors:

Jeannette Nardelli: jeannette.nardelli@inserm.fr

Pierre Gressens: pierre.gressens@inserm.fr

1 Lead contact : Jeannette Nardelli

SUMMARY

A distinctive feature of the neocortical development is the highly coordinated production of different progenitor cell subtypes, which are critical for ensuring adequate neurogenic outcome and the development of normal neocortical size. To further understand the mechanisms that underlie neocortical growth, we focused our studies on the microcephaly gene *Mcph1*, and we report here that *Mcph1* 1) exerts its functions in rapidly dividing apical radial glial cells (aRGCs) during mouse neocortical development stages that precede indirect neurogenesis, 2) is expressed at mitochondria; and 3) controls RGC proper proliferation and survival, potentially through crosstalk with cellular metabolic pathways, involving stimulation of mitochondrial activity via VDAC1/GRP75, AKT/HK2/VDAC1 and of glutaminolysis via ATF4/PCK2. We thus currently report the description of a MCPH gene implication in the interplay between bioenergetic pathways and neocortical growth, thus pointing to alterations of cellular metabolic pathways, in particular of glutaminolysis, as possible cause of microcephalic pathogenesis.

INTRODUCTION

The evolutionary expansion of the mammalian neocortex (nctx) underlies the development of sophisticated cognitive functions, culminating in humans. This evolutionary hallmark has raised interesting issues with regard to the mechanisms that determine neocortical size and how these mechanisms were adapted to drive neocortical expansion. Nctx size is determined by the neuronal output, which is governed by the proliferative capacity of neural progenitor cells. Three cellular subtypes of neural progenitors emerge progressively in tight coordination with neocortical development. The primary neuroepithelial cells amplify by symmetric divisions and give rise to apical radial glial cells (aRGCs), which divide at the ventricular border and constitute the ventricular zone (VZ). Basal progenitors, including intermediate progenitor cells (IPCs) and basal RGCs (bRGCs), arise from aRGC by asymmetric divisions and populate the subventricular zone (SVZ), in which they divide to generate neurons (Dehay et al., 2015; Florio and Huttner, 2014; Lui et al., 2011). Hence, all neuronal cell types arising in the nctx belong to the aRGC lineage and any alteration of aRGC production is expected to have a profound impact on the neocortical size. The greater neurogenic output seen in the gyrencephalic nctx of humans and non-human primates, compared to lissencephalic nctx of lower species like rodents, is thought to rely on the formation of a further germinative layer in the SVZ, called the outer SVZ (OSVZ), in which neurogenesis is extended by further proliferation of neural progenitors (Betizeau et al., 2013; Kalebic et al., 2019; Martinez-Martinez et al., 2016; Nowakowski et al., 2017).

Despite advances in the characterization of the molecular cues governing intrinsic functions in specific neural progenitor subtypes (Florio et al., 2015; Kalebic et al., 2019; Nowakowski et al., 2017), the molecular pathways controlling the transition and proper balance between these subtypes remain unclear. Recently, several lines of evidence have implied bioenergetics pathways in the fate determination of neural progenitor. During neocortical development, the actively proliferating aRGCs stimulate glycolysis, whereas neuronal differentiation by indirect neurogenesis requires a switch to oxidative phosphorylation (Lange et al., 2016; Wagenfuhr et al., 2015; Zheng et al., 2016). The fate of

early aRGCs is also influenced by the PERK (Protein kinase RNA-like endoplasmic reticulum Kinase)/ATF4 arm of UPR (Unfolded Protein Response), which promotes the birth of pioneer neurons by direct neurogenesis, and inhibits indirect neurogenesis (Frank et al., 2010; Laguesse et al., 2015). How bioenergetic pathways mechanistically control progenitor behavior with respect to proliferation rate, mode of division and survival, is not clear.

In this context, non-syndromic genetic autosomal recessive primary microcephaly (MCPH) has proved to be a powerful research model to investigate fundamental mechanisms that maintain neural progenitor homeostasis in the developing nctx. All of the hitherto identified MCPH genes (MCPH1-25) play a role in cell division (Duerinckx and Abramowicz, 2018; Jayaraman et al., 2018). To further elucidate the mechanisms responsible for microcephaly pathogenesis, which in turn may provide insight into the mechanisms regulating the size of the nctx, we focused our research on *MCPH1*, a MCPH gene with multifaceted functions (Jackson et al., 1998; Liang et al., 2010; Peng et al., 2009; Pulvers et al., 2015). In mouse neural progenitors, *Mcph1* controls the coupling between the centrosome cycle and the entry into M-phase through the Cdc25b/Chk1 pathway (Gruber et al., 2011). Here, we show that MCPH1 is expressed at mitochondria and directly influences mitochondrial functions by interfering with the VDAC1/GRP75 pathway and notably, by stimulating glutaminolysis via the ATF4/PCK2 pathway. We thus reveal that *Mcph1* is involved in the crosstalk between bioenergetic pathways, an essential function for the proliferation and survival of neocortical progenitors.

RESULTS

Mcph1 expression in aRGCs declines with the onset of indirect neurogenesis

First, we determined the dynamic of Mcph1 expression in progenitors during mouse neocortical development. Immunofluorescence (IF) performed between embryonic day (E) 10.5 and E16.5 illustrated clear Mcph1 expression in the cytoplasm of aRGCs in the VZ (**Figures 1A-G**). More concentrated at the apical side of these cells, as indicated by co-localization with apical proteins, such as Par3 (Bultje et al., 2009) and Dock7 (Yang et al., 2012), this expression remained weak at more basal positions where APC staining extended (**Figure 1G**). Of note, no expression was detected in the nucleus or at the centrosome (**Figure 1D**). Furthermore, Mcph1 expression overlapped with that of RC2, a post-translationally modified nestin isoform specifically expressed in mouse aRGCs (Park et al., 2009) (**Figure 1E**), not with that of Tbr2 (**Figure 1F**). This discrimination between Mcph1 and Tbr2 expression was further supported by the decrease in Mcph1 expression from E10.5 to E13.5, and no detection of this expression on E14.5 (**Figures S1A-B)** and E16.5 (**Figure S1D**) nctx sections or in E14.5 whole-mount nctx (**Figure S1C**) further stained with γTubulin antibodies for the better visualization of mitotic cells at the ventricular border. This limited time-window of *Mcph1* expression was confirmed at the RNA level by RNA *in situ* hybridization, as no signal was detected in E14.5 and E16.5 nctx (**Figure S1E**).

Taken together, these results indicate that Mcph1 is primarily expressed in aRGCs in a decreasing manner from E10.5 to E13.5. The discordance with a previous study showing Mcph1 expression at E15.5 (Gruber et al., 2011) can be explained by the very sensitive method that was used, indicating an extremely lower level of Mcph1 expression compared to earlier stages that we examined here.

In contrast to our findings in mice, MCPH1 expression was observed at later stages of human neocortical development, such as post-conception weeks (PCW) 11 **(Figures 1H-K)** and PCW13 (data not shown). This expression was primarily detected in a subset of RGCs in both the VZ and OSVZ, as illustrated by its prominent overlapping with PAX6 expression compared to TBR2 (**Figures 1J** and **1L**). Of note, in contrast to mice, MPCH1 was expressed in nuclei in addition to the cytoplasm.

To consolidate our expression data in human, we analyzed transcriptomic data from the Human BrainSpan Atlas (Kang et al., 2011; Pletikos et al., 2014) and observed that MCPH1 expression is highest during the earliest stages of neocortical development, before the PCW16 stage, and then progressively declines (**Figure S1F**).

Collectively, these expression data show that MCPH1 expression peaks at the early stages of neocortical development and is primarily associated with RGCs, both in humans and mice. They raise the question of a specific role of *MCPH1* in RGCs.

***Mcph1* conditional deletion in the mouse nctx induces microcephaly**.

To answer this question, we generated *Mcph1*$^{lox/lox}$*; Emx1*$^{kiCre/+}$ mice (cKO) with specific *Mcph1* inactivation in neocortical progenitors, and we phenotypically compared these mutant mice to *Mcph1*$^{lox/lox}$ (Ct) mice. No Mcph1protein expression was detected in the lateral nctx of E12.5 cKO embryos, which gives rise to the neocortical neurons, whereas Mcph1 expression was seen in the medial nctx (**Figure S2A**), probably due to lower efficiency of *Mcph1* excision in medial area. The cKO mice developed microcephaly, underlined by the reduction of brain weight and of longitudinal and lateral neocortical size (**Figures 2A** and **2B**). To further characterize the morphogenic defects of the cKO nctx, we used two approaches for neuron BrdU birthdating: first, the double injection of pregnant mice with BrdU at E12.5 and E13.5 to trace the earliest layer VI neurons Tbr1+ and analyze their outcome at post-natal day (P) 0; and second, the BrdU injection at E14.5 to trace neurons of layers V to II and analyze them at P5, when their migration is complete. DAPI-staining coupled with layer neuron marker and BrdU double IF allowed us to determine: 1) the global number of neurons and BrdU distribution within the cortical plate; 2) the number of neurons and BrdU distribution in each neuron layer.

Following BrdU injection at E12.5 and E13.5, P0 nctx displayed a decrease in the total number of neurons in cKO versus Ct nctx (**Figures S2B** and **S2C**), but no significant change in the total number of BrdU positive nuclei and the distribution of Tbr1+ and Tbr1+BrdU+ neurons (**Figure S2C**). After BrdU injection at E14.5, the significant decrease in the total number of neurons in the P5 cKO versus Ct nctx was now associated with a global reduction of BrdU incorporation (**Figures 2C**

and **2D**). Again, the number of Tbr1+ neurons was similar in Ct and cKO nctx and, as expected, these neurons were barely traced by BrdU (**Figures 2C** and **2D**). In contrast, the neuronal outcome in the layers V to II and the global BrdU distribution were significantly decreased (**Figures 2C** and **2D**), whereas BrdU incorporation in each layer was not impacted (**Figure 2D**). This result can be explained by dilution of the global BrdU decrease in the different layers.

Collectively, these data suggested that neurogenesis proceeds normally between E12.5 and E13.5, whereas neuron arising is impaired later on. They are consistent with the decrease in upper neurons reported in the *Mcph1* full knock out nctx (Gruber et al., 2011), and suggest a possible premature exhaustion of progenitors.

***Mcph1* mutation induces early mitotic anomalies associated with progenitor cell death**

In regard with these results, we examined progenitors in E12.5 Ct and cKO nctx. Double IF of Tpx2, a protein interacting with spindle microtubules (Gruss et al., 2002), and Aurora kinase B (AurkB), a cell cycle kinase that localizes to microtubules near kinetochores (Terada et al., 1998), evidenced frequent disorganized mitotic spindles at the ventricular border of *Mcph1* cKO nctx (**Figure S2D**): 24 abnormal mitoses among 53 counted in cKO (66%) versus 2 among 35 in Ct nctx (6%). Phospho-Histone H3 (PH3) and cleaved Caspase-3 (CC3) double IF indicated that these defects were associated with ab-ventricular mitoses and cell death (**Figure 2E**). As shown in **Figure 2F**, CC3 was expressed in long cellular processes evoking RGCs, not in Tbr2+ IPCs, which suggested that cell death impacted primarily RGCs. Further analysis at E11.5, E14.5 and E16.5 established that cell death in cKO nctx was largely prominent at E12.5 (**Figure 2G**), which was corroborated with a decrease in ventricular mitoses (PH3+), specific at E12.5 (**Figure 2H**). These results were consistent with the time-window of Mcph1 expression.

Next, to assess the impact of these mitotic defects on progenitor production, we examined the distribution of BrdU acute incorporation in aRGCs (Pax6+) and of Tbr2+ IPCs newly born in the VZ (delineated by Pax6 expression) or settled in the SVZ (no Pax6 expression), as indicated in **Figure S2E**. The distribution of Pax6+ and Pax6+ BrdU+ cells was comparable in E12.5 Ct and cKO VZ (**Figure S2F**), but, in contrast, decreased significantly at E14.5 and E16.5 (**Figures S2G** and **S2H**).

Similar in E12.5 Ct and cKO VZ/SVZ (**Figure S2F**), the IPC population was reduced in the E14.5 cKO VZ (**Figure S2G**). This defect seemed to be compensated in the E16.5 cKO VZ, but was associated with a decrease in IPCs in the E16.5 cKO SVZ (**Figure S2H**).

Collectively, these results indicate that the progenitor cell death peaking in the E12.5 cKO VZ is related to mitotic anomalies, progressively alters the aRGC pool and results in lower production of IPCs, which can account for the impaired upper layer neuron production afore described.

***Mcph1* interacts with cellular metabolic pathways and is localized at mitochondria.**

Next, to gain insight into how *Mcph1* inactivation affects the cell division and survival of neocortical progenitors at the molecular level, we took advantage of primary cultures of mouse neural progenitor cells (NPCs) that we derived from nctx dissected from E12.5 wild type (WTNPCs) and *Mcph1* full knock out (KONPCs) embryos, to ensure *Mcph1* deletion in all cells. Following RNA sequencing, gene expression profiling analyses revealed differential expression of genes controlling the cell cycle in KONPCs. For instance *Cdk1* and *Chek1*, genes already known as being regulated by *Mcph1* (Gruber et al., 2011), were significantly down regulated (fold change FC=5.13, adjusted *p*-value=$8.53\text{x}10^{-3}$ for *Cdk1*; FC=5.08 adjusted *p*-value=$1.03\text{x}10^{-2}$ for *Chek1*). Moreover, genes related to metabolic pathways, including 93 nuclear genes encoding mitochondrial proteins, also stood out among differentially expressed genes, highlighting oxidative phosphorylation as one of the most affected pathway (**Figure 3A; Table S1**)**.** This unexpected finding indicated a large impact of the *Mcph1* mutation on bioenergetics pathways and was an incentive to explore the interplay between *Mcph1* and such pathways.

First, the sub-cellular distribution of the Mcph1 protein in WTNPCs established by IF suggested a possible localization of Mcph1 at the mitochondria or near the outer membrane (for simplicity, we will keep mentioning mitochondrial localization to refer to both situations). This was confirmed by 1) the overlapping distribution of Mcph1 and either SDHA (a protein of the respiratory chain complex II) or MitoTracker Deep Red (MitoT), a mitochondrial fluorescent probe (**Figure 3B**); 2) importantly, evidence for this localization in aRGCs provided by gold-immunostaining and electronic microscopy analysis (**Figure 3C**); and 3) mitochondrial targeting of the transiently

expressed HA-tagged human MCPH1 protein in mouse NPCs (**Figure 3D**). Of note, MCPH1 mitochondrial localization was also observed in human NPC (hNPC) (**Figure 3E**).

Mcph1 inactivation impacts mitochondrial functionality

Altogether, these results raised the hypothesis of a link between *Mcph1* and mitochondria functionality. With this regard, we first checked the impact of the *Mcph1* deletion on mitochondrial integrity by comparing the morphology of the mitochondrial network in WTNPCs and KONPCs. When labeled with MitoT and a SDHA antibody, mitochondria appeared smaller and more fragmented in KONPCs (**Figure 3F**). This higher fragmentation was not related to a loss in mitochondrial membrane amount, as indicated by 1) ELISA quantification of the complex I of the respiratory chain (**Figure 3G**); 2) similar expression levels of VDAC1, a major mitochondrial protein, analyzed by Western blotting (**Figure 3H**); and 3) morphometric analyses by electronic microscopy, indicating no significant change of the total mitochondrial surface relative to the cytoplasm, but an increase in mitochondria number (**Figure 3I**).

To determine whether the higher mitochondrial fragmentation in KONPCs was a sign of mitochondrial activity alteration, we measured the activity of respiratory chain enzymes in NPCs maintained either in complete medium with Glucose, Pyruvate and Glutamine (GPGln), or in medium deprived of either Glucose (PGln) or both Glucose and Pyruvate (Gln) to challenge mitochondrial activity. We thus measured the activity of the rotenone-sensitive NADH quinone reductase (CI), the malonate-sensitive succinate cytochrome *c* reductase (SCCR, CII+CIII), the glycerol cytochrome *c* reductase (GCCR, G3PDH+CIII), the Decylubiquinol cytochrome *c* reductase (QCCR, CIII), the cyanide-sensitive cytochrome *c* oxidase (Cox, CIV) and the oligomycine-sensitive ATPase (CV). In GPGln medium, each activity was comparable between KONPCs and WTNPCs (**Figures 4A-F**). In PGln medium compared to GPGln medium, the tested activities, except for SCCR in WTNPCs, tended towards general decrease, although not significant, in both WTNPCs and KONPCs (**Figure 4A-F**). Comparing activities between WTNPCs and KONPCs in either PGln or Gln medium, we found a significant decrease in ATPase activity (**Figure 4F**) in KONPCs, whereas other activities remained

unchanged (**Figures 4A-E**). The significant increase in SCCR enzymatic activity observed in Gln medium (**Figure 4A**) suggested attempt of cells to enhance mitochondrial biogenesis.

Overall these results indicate that the *Mcph1* deletion significantly affects ATPase activity, underlying mitochondrial dysfunction. This dysfunction is masked in presence of glucose, a well-known phenomenon (Benit et al., 2019).

Since mitochondrial activity is modulated by calcium concentration (Cardenas et al., 2010), we then questioned whether the observed mitochondrial deficiency was related to reduced calcium availability. We thus transiently transfected glucose-deprived NPCs with mito-GEM-GECO1, a fluorescent protein reporter of mitochondrial calcium (Zhao et al., 2011) (**Figure 4G**) and measured emission ratios. We thus found significantly lower calcium amount in KONPCs (**Figure 4H**), underlining alteration of the mitochondrial activity.

Next, we addressed whether the mitochondrial defects evidenced in KONPCs upon low carbon source availability were related to compromised cell survival. By CC3 IF and counting positive cells, WTNPCs displayed elevated cell death in Gln medium only (**Figure 4I**). In KONPCs, cell death was clearly more pronounced in both PGln and Gln medium (**Figure 4I**). Notably, analysis of ROS (Reactive Oxygen Species) production by FACS (Fluorescence Activated Cell Sorting) did not show any difference between KONPCs and in PGln (**Figures S3A** and **S3B**), suggesting that cell death in KONPCs was not related to higher ROS production.

Together these results indicated that exposure to low carbon source availability was more critical for KONPCs than WTNPCs. To determine whether deficiency of key metabolic enzymes involved in replenishing the tricarboxylic acid (TCA) cycle could account for this difference, we next assessed the activities of the following enzymes: 1) Hexokinases I-IV and lactate dehydrogenase (LDH), key enzymes of glycolysis; 2) Glucose-6-phosphate dehydrogenase (G6PDH), a rate-limiting enzyme in the pentose-phosphate pathway and the synthesis of nucleic acids; and 3) IDH3 and IDH1/2, respectively NAD^+- and $NADP^+$-dependent IDH (isocitrate dehydrogenase), enzymatic isoforms catalyzing the oxidative decarboxylation of isocitrate to produce α-ketoglutarate. These enzymatic activities did not vary significantly between WTNPCs and KONPCs (**Figures 4J, 4K)** and

S3C-E), and the mitochondrial defects of *Mcph1* KO NPCs could not be explained by deficiency of these enzymes.

***Mcph1* influences mitochondrial activity via glutaminolysis.**

We next considered another key pathway often solicited to sustain the TCA cycle and mitochondrial activity upon low glucose availability or high energetic demand, which is phosphoenolpyruvate (PEP) production from glutamine through the activity of mitochondrial phosphoenolpyruvate carboxykinase, PEPCK-M or PCK2. In addition to driving the TCA cycle, Glutamine-derived PEP or glutaminolysis can fuel multiple biosynthetic processes, critically contributing to cell growth and survival during stress (Mendez-Lucas et al., 2014; Vincent et al., 2015). With this regard, we demonstrated PCK2 expression in WTNPCs (**Figure 5A**) and down regulation of this expression in KONPCs, consistent with our transcriptomic data (FC=2,72, adjusted *p*-value=5,65x10^{-3}). Importantly, PCK2 expression was markedly increased in WTNPCs upon PGln or Gln medium, but remained very low in KONPCs (**Figure 5B**). Furthermore, our IF analysis indicated that PCK2 expression decreased between E10.5 and E14.5 (**Figures 5C-E**), and, of note, was down regulated in E10.5 KO nctx (**Figure 5C**). These results uncover that mouse neural progenitors solicit PCK2 and *a fortiori* glutaminolysis, and that Mcph1 is involved in PCK2 regulation. In addition, illustration of PCK2 expression in human neocortical progenitors, in hNPCs and in the VZ of a PCW11 fetal nctx, (**Figures S4A and S4B,** respectively), suggests that this regulation may occur in Human as well. To strengthen this finding, we addressed whether ATF4, a transcription factor able to activate *PCK2* transcription (Mendez-Lucas et al., 2014), was also misregulated in KONPCs. In line with transcriptomic analyses indicating a 2.32 fold decrease in *ATF4* expression (*p*-value=2,11x10^{-2}), the basal expression of the ATF4 protein was lower in KONPCs compared to WTNPCs, and was not stimulated in KONPCs in PGln and Gln medium, as in the cas of PCK2 (**Figure 5F**).

Previous studies have reported that ATF4 is expressed, like Mcph1, in aRGCs before the bulk of indirect neurogenesis (Franck et al. 2010; Laguesse et al. 2015) and regulates progenitor proliferation and the stimulation of the PERK arm of the Unfolded Protein Response (UPR), (Frank et al., 2010; Godin et al., 2016; Laguesse et al., 2015). Since HSPA5/Bip1/GRP78 is the upstream

regulator of UPR, we examined the expression of this protein and found a significant increase in KONPCs upon Gln versus GPGln medium (**Figure 5G**), indicating a possible stimulation of UPR.

Altogether our results show that *Mcph1* may participate in glutaminolysis stimulation via the ATF4/PCK2 pathway.

Glutaminolysis contributes with glycolysis to fuel the cell cycle of NPCs.

In this context, we next assessed the respective influence of glycolysis and glutaminolysis on the proliferation of WTNPCs and KONPCs. By FACS analysis of the cell cycle, we examined the impact of the following metabolic inhibitors: 2-DG (2-Deoxyglucose), a glucose competitor that inhibits the first step of glycolysis by blocking Hexokinases; UK5099 (2-Cyano-3-1-phenyl-1H-indol-3-yl-2-propenoic acid), an inhibitor of the mitochondrial pyruvate carrier; BPTES (Bis-2-5-phenylacetamido-1,3,4-thiadiazol-2-yl ethyl sulfide), a glutaminase inhibitor (**Figure S5A**). Analyzing cellular DNA content and EdU incorporation during the S phase allowed us to determine the distribution of NPCs in G0/G1, S and G2/M phase. BPTES and UK5099 alone had no effect on the on both WTNPCs and KONPCs (data not shown). 2-DG, alone or coupled to BPTES did not impact the percentage of WTNPCs and KONPCs in G0/G1, but caused an increase in this percentage in KONPCs when it was coupled to UK5099 (**Figure 6A** and **6B**). In contrast, 2-DG caused a decrease in the percentage of NPCs in the S phase, potentially more significant in KONPCs compared to WTNPCs (based on *p* values; **Figures 6A and 6C**). Interestingly, addition of BPTES or UK5099 accentuated this decrease in WTNPCs, not in KONPCs. In counterpart, 2-DG caused an increase in cells in G2/M, more pronounced in WTNPCs (**Figure 6D**).

These results suggest that glutaminolysis and mitochondrial activity may participate, in addition to glycolysis, in energetic supply during the S phase, and support the notion that these two functions are altered in KONPCs.

To further investigate the impact of metabolic inhibitors in WTNPCs and KONPCs, we compared the levels of transcriptional activation of *PCK2*, *ATF4*, *GLS1* (Glutaminase 1, expressed in the brain and converting glutamine to glutamate) (Olalla et al., 2002), and *GLUD1* (glutamate dehydrogenase, converting glutamate to α-ketoglutarate) (Shashidharan et al., 1994). 2-DG alone

induced an increase in *PCK2* expression in WTNPCs, not in KONPCs (**Figure S5C**), consistently with the observed protein expression variations and with the hypothesis of glutaminolysis stimulation upon glucose and pyruvate deprivation in WTNPCs. This increase in *PCK2* activation was maintained by addition of BPTES or UK5099, indicating that these inhibitors do not impact *PCK2* transactivation. In contrast to *PCK2* and to the increase in the ATF4 protein expression observed upon glucose and pyruvate deprivation, 2-DG did not affect *ATF4* RNA expression (**Figure S5B**), which can be explained by the important role of post-translational modifications in the regulation of ATF4 expression (Lassot et al., 2001). Furthermore, 2-DG caused a decrease in *GLS1* (**Figure S5D**) and *GLUD1* (**Figure S5E**) expression, indicating that the transcriptional activation of *PCK2* is regulated independently of *GLS1* and *GLUD1*.

Mcph1 interacts with VDAC1 and modulates its activity via GRP75 and HK2

To gain insight into the modalities of Mcph1 recruitment at mitochondria and into how this localization impacts mitochondrial activity, we searched for potential MCPH1 mitochondrial molecular partners by mining data obtained by co-immunoprecipation (Co-Ip) experiments (Liu et al., 2017). Following identification of HSPA9/GRP75 as a potential partner of MCPH1, Mcph1 and GRP75 co-localization was observed in mNPCs by double IF (**Figure S6A**). Importantly, we demonstrated that the two MCPH1 C-terminal (C-ter) BRCT domains mediated the MCPH1 and GRP75 interaction by performing Co-IP with transiently expressed HA-tagged complete or deleted MCPH1 proteins and Flag-tagged GRP75 (**Figure 7A**). In addition, KONPCs displayed a lower GRP75 expression than WTNPCs (**Figure 7B**). Altogether these results indicate a strong interplay between Mcph1 and GRP75.

GRP75 is regulated by glucose and interacts with the Voltage-dependent anion channel 1 (VDAC1), a protein found in the outer mitochondrial membrane and important for the exchange of metabolites between mitochondria and the intracellular environment (Betz et al., 2013; Flachbartova and Kovacech, 2013; Szabadkai et al., 2006). In particular, GRP75 bridges VDAC1 to Inositol-triphosphate receptor (IP3R) to allow calcium flux from endoplasmic reticulum into mitochondria and stimulation of the TCA cycle (Betz et al., 2013; Szabadkai et al., 2006). This raised the hypothesis

of possible interaction between MCPH1 and VDAC1 too, which we assessed by expressing HA-tagged MCPH1, either full length or deleted of the two C-ter BRCT domains, in HEK293T cells, and by performing Co-IP. Considering the amounts of the co-immunoprecipated VDAC1 and the input of each MCPH1 protein, VDAC1 interaction seemed stronger with the full-length MCPH1 protein (**Figure S6B**), suggesting that the two C-ter BRCT domains are important for interaction with VDAC1 as with GRP75. We then examined the modalities of Mcph1/VDAC1/GRP75 interactions by performing series of Proximity Ligation Assays (PLA) in NPCs. In WTNPCs, we found that Mcph1 interacts more robustly with VDAC1 than with GRP75 in GPGln medium, and that Mcph1 interaction with VDAC1 is markedly enhanced in both PGln and Gln medium, whereas interaction with GRP75 increases significantly in Gln medium only (**Figures 7C** and **7D**). These increases were not merely due to higher expression levels of GRP75 and VDAC1, since protein expression did not change between conditions (**Figure S6C**). Second, these interactions were detected *in vivo* on sections of mouse E10.5 nctx, again with a higher dot distribution in the case of Mcph1 and VDAC1 than Mcph1 and GRP75 (**Figure 7H**). Third, MCPH1 interaction with VDAC1/GRP75 is similarly modulated in hNPCs (**Figures 7E** and **7F**). Importantly, interaction between GRP75 and VDAC1 was mainly detected in WTNPCs maintained in Gln medium, and was not observed in KONPCs (**Figure 7G**), despite higher expression of two proteins in PGln and Gln medium (**Figure S6C**). Interestingly, these data indicated that Mcph1 influences VDAC1/GRP75 interaction.

Altogether, these results uncovered that Mcph1 interacts with the VDAC1/GRP75 pathway. They prompted us to address whether Mcph1 also interferes with the Hexokinase-2 (HK2) pathway, which attenuates VDAC1 activity by stimulating glycolysis via Glucose-6-Phosphate (G6P) production (Betz et al., 2013; Hou et al., 2015). Interestingly, by performing PLA, we provided evidence for HK2/VDAC1 interaction in KONPCs, not in WTNPCs (**Figure S6D**). This difference was not related to higher expression of HK2 in KONPCs **(Figure S6E)**. Two main mechanisms control HK2 binding to VDAC1: 1) primary HK2 phosphorylation by Akt (Roberts et al., 2013); and 2) negative feedback exerted by high levels of G6P (Hou et al., 2015). Hence, stimulation of HK2 binding in KONPCs raised the question of a possible higher Akt activation in these cells. Akt is activated by phosphorylation of two residues, Serine (S) 473 and Threonine (T) 308, by mTOR2 and

PDPK1 (3-Phosphoinositide Dependent Protein Kinase 1), respectively (Beg et al., 2017). By Western blotting, we found that 1) the expression of total Akt did not significantly vary between KONPCs and WTNPCs, whatever the culture condition; 2) the expression of pAkt S473 appeared to be increased, although not significantly, in KONPCs in PGln and Gln medium; and 3) pAkt T308 expression was in contrast markedly elevated in KONPCs, not in WTNPCs, upon PGln and Gln medium. Importantly, the pAkt T308 stimulation in KONPCs was corroborated with that of PDPK1 (**Figure S6F**).

Taken together our results indicate that Mcph1 can influence VDAC1 activity via two pathways: stimulation of GRP75 binding and constraint of HK2 binding via inhibition of Akt activation.

DISCUSSION

MCPH1 has been involved in a variety of basic functions related to the cell cycle, such as chromosome segregation, double strand DNA repair, and DNA recombination during meiosis. Altogether, these functions are essential for the maintenance of genomic integrity, and their alteration can promote tumorigenesis or infertility (Liang et al., 2015; Liang et al., 2010). Despite the clear implication of *MCPH1* mutations in human microcephaly (Jackson et al., 1998; Pulvers et al., 2015), studies exploring the functions of the gene during neocortical development and explaining how *MCPH1* deficiency can lead to microcephaly remain limited. A previous study analyzing an *Mcph1* full knock out mouse line indicated that *Mcph1* promotes the symmetric division of neuroprogenitor cells via the Chk1/Cdc25b pathway, which controls the coupling of the centrosome cycle with the entry into the M-phase of the cell cycle (Gruber et al, 2011). Here, we provide information in regard with the temporality of *Mcph1* implication in neocortical development and the mechanisms underlying this implication.

In this respect, we present a detailed expression pattern of Mcph1 in the mouse developing nctx, showing that Mcph1 expression is restricted to aRGCs during a time-window corresponding to the prevalence of the symmetric division of these cells, and thereby strengthening the notion that Mcph1 promotes this cell division mode. These data and the lack of expression of Mcph1 at the centrosome distinguish *Mcph1* from other MCPH genes, in particular such as *Wdr62* (*MCPH2*) (Chen et al., 2014), *Cdk5Rap2* (*MCPH3*) (Issa et al., 2013), *Aspm* (*MCPH5*) (Fish et al., 2006), *Cenpj* (*MCPH6*) (Garcez et al., 2015), whose expression at the centrosome is maintained in the mouse VZ and/or SVZ during all stages of mouse neocortical development.

Interestingly, a comprehensive analysis of expression data from the Human BrainSpan Atlas (Kang et al., 2011; Pletikos et al., 2014) also emphasized a prominent *MCPH1* expression during the earliest stages of the human neocortical development, and furthermore indicated that, in contrast to mice, this expression is maintained at later developmental stages, albeit at lower levels. According to our data obtained at PCW11 and 13, this later expression is related to a subset of aRGCs and bRGCs in the VZ and OSVZ respectively. At these stages indirect neurogenesis is well underway, however

aRGCs and bRGCs continue to undergo frequent symmetric divisions (Betizeau et al., 2013; Dehay et al., 2015; Florio and Huttner, 2014; Lui et al., 2011; Martinez-Martinez et al., 2016). Altogether, these data raise the challenging question of whether MCPH1 expression in human bRGCs promotes their symmetric division, thus facilitating their expansion in the OSVZ as well. Furthermore, the expression of MCPH1 in the nucleus of human neural progenitors suggests that the human protein assumes further functions that may also participate in their expansion. This nuclear localization in humans may rely on amino acid substitutions existing in the three characterized nuclear localization sequences of the murine and human protein (Gavvovidis et al., 2012) or on specific post-translational modifications that would selectively control translocation of the human protein to the nucleus. This hypothesis is supported by the poor cross-reaction that we observe between antibodies raised against the human and the mouse MCPH1 proteins (data not shown). The molecular bases of this differential subcellular localization will be an interesting issue to address.

Despite the short time window of *Mcph1* expression, its deletion in neocortical progenitors was sufficient to induce microcephaly. Neuron birth dating experiments showed that the primary layer VI Tbr1 neurons are produced to a similar extent in cKO and Ct nctx, whereas the outcome of the upper neurons is affected, which corroborates with data obtained with the Mcph1 full knock-out mice (Gruber et al., 2011). This situation can be explained by primary loss of progenitors due to the cell death (this study), and by an imbalance in asymmetric neurogenic divisions (Gruber et al., 2011) contributing to the generation of Tbr1 neurons, both defects finally leading to exhaustion of the progenitor pool. These hypotheses are supported by several lines of data: 1) a peak of cell death observed in the E12.5 cKO VZ; 2) a reduction of the longitudinal size of cKO newborn nctx, such reduction being supposed to rely on impaired expansion of RGCs (Florio et al., 2014); 3) a decrease in Pax6+ progenitors proliferating in the E14.5 and E16.5 cKO VZ, as demonstrated by acute BrdU incorporation; 4) a diminution of IPCs arising in the VZ at E14.5 and settled in the SVZ at E16.5; 5) a decreased distribution of the cortical neurons traced by BrdU injection at E14.5.

Unexpectedly for an MCPH gene, comparative gene expression profiling between WTNPCs and KONPCs uncovered a crosstalk between *Mcph1* and metabolic pathways. The emergence of oxidative phosphorylation as one of the most affected pathways in KONPCs and the uncovering of the

MCPH1 localization at mitochondria solidified the notion that this crosstalk involves mitochondria, which our study supports in different ways.

The fact that higher mitochondrial segmentation in KONPCs was not associated with loss of global mitochondrial amount indicated that this fragmentation is not related to mitophagy (Chen and Chan, 2009). Based on ATPase deficiency evidenced in PGln and Gln medium, this fragmentation is rather associated with mitochondrial activity alteration. The lack of significant impact of the *Mcph1* mutation on key glycolytic enzymes, such as HK2 and LDH, indicates that insufficient replenishing of the TCA cycle due to glycolysis impairment cannot account for the mitochondrial activity alteration. Instead, our data have related this alteration to a deficiency of the ATF4/PCK2 pathway, which triggers glutaminolysis, a further pathway participating in replenishing the TCA cycle and essential for active cell proliferation or survival in the context of metabolic stress (Colombo et al., 2011; Mendez-Lucas et al., 2014; Vincent et al., 2015). Several lines of data emphasize this implication of glutaminolysis in neocortical progenitors. First, during mouse neocortical development, the functions of the ATF4 protein, *PCK2* transactivator (Mendez-Lucas et al., 2014), take place during the time-window of Mcph1 and PCK2 expression, before the launch of indirect neurogenesis (Frank et al., 2010; Laguesse et al., 2015), which is consistent with a possible crosstalk between the three genes. The clear down-regulation of both ATF4 and PCK2 in KONPCs and of PCK2 in the E10.5 KO nctx strongly supports that Mcph1 regulates the ATF4/PCK2 pathway. Furthermore, our data indicate that the mis-regulation of this pathway in KONPCs is associated with impaired glutaminolysis. This notion is based on the differential impact of BPTES addition to 2-DG on the cell cycle between WTNPCs and KONPCs, and the higher cell death induced in KONPCs in Gln medium. On the basis of data reporting glutaminolysis solicitation for normal progression of cell division from late G1 (Colombo et al., 2011) and of our present data indicating that glutaminolysis inhibition strengthens the effect of 2-DG on the S phase, we suggest that glutaminolysis is required in addition to glycolysis for normal cycle progression in neuroprogenitors.

MPCH1 interaction with VDAC1/GRP75 appears to be an important clue for understanding the interplay between MCPH1, glycolysis, mitochondria and glutaminolysis. The prominent MCPH1 interaction with VDAC1 compared to GRP75 can result from the larger distribution of VDAC1 at

mitochondria and indicates that this interaction can occur independently of GRP75. According to our data, Mcph1 stimulates VDAC1 activity in two ways. First, the disruption of GRP75 and VDAC1 interaction in absence of Mcph1 infers that Mcph1 is required for this interaction to occur in neural progenitors, either by facilitating GRP75 binding to VDAC1, or by a positive control of GRP75 expression, as suggested by the decrease in this expression in KONPCs. The lower mitochondrial calcium uptake associated with this disruption reflects functional alteration of VDAC1, compromising cell survival, as underlined by the higher cell death observed in KONPCs in PGln and Gln medium and consistently with previous studies involving VDAC1 in cell survival (Szabadkai et al., 2006). Second, Mcph1 participates in sustaining VDAC1 activity by inhibiting the PDPK1/Akt/HK2 pathway, thus preventing VDAC1 inhibition by HK2 binding (Hou et al., 2015; Roberts et al., 2013). Of note, activated Akt is also supposed to disrupt the IP3R/GRP75/VDAC1 complex (Betz et al., 2013), and Mcph1 may facilitate GRP75 and VDAC1 interaction by constraining Akt activation.

Altogether, our studies have uncovered a role of MCPH1 at the intersection of bioenergetics pathways that participate in the homeostasis of early neocortical neural progenitor cells, which, due to intense proliferation, sustain active biogenesis and high energetic demand. To fulfill this demand, aRGCs have been shown to take advantage of glycolysis (Lange et al. 2016). Collectively, our data indicate that glutaminolysis may be critically solicited in addition to glycolysis to respond to high metabolic challenges that they are exposed to *in vivo* during rapid periods of proliferation. The impact of low glucose availability or glutaminolysis deficiency on microcephaly etiology is not known. In this regard, our study opens new windows to explore the mechanisms underlying microcephalic pathogenesis and will help attract the attention of clinicians and geneticists on possible implication of bioenergetics alterations in such etiology.

ACKNOWLEDGMENTS

We are grateful to Kayi Li (Baylor College of Medicine, Houston) for the *Mcph1* KO mice. We thank Jeremy Pulvers, Yoko Arai, Sylvie Berrard and Takashi Namba for critical reading of the manuscript,

Fanny Coulpier and the Genomics Platform at IBENS, Ecole Normale Supérieure, Paris, for generating transcriptomes, GenoSplice technology for transcriptome analysis and Melina Devos and Pierrette Young-Ten for animal care and genotyping. This work was supported by grants from Inserm, Paris Diderot University, ERA-NET Neuron (MicroKin), EU grant HEALTH-2011/DEVELAGE, Investissement d'Avenir-ANR-11-INBS-0011, ARC (Association pour la Recherche sur le Cancer), Roger de Spoelberch and Grace de Monaco Foundations.

AUTHOR CONTRIBUTIONS

J.N., P.G. and P.R. designed the research; N.J, S.C, P.B, J.G-J, X.L., S. J, V.F, E.M, T.H, A.D-D, Z.C, S.L, C.V-P, H.A-B, P.R, J.N performed the research, analyzed and formatted data; J-F.O provided human tissues; Z-Q.W provided information on MCPH1 partners screening, J.N, P.G, P.R and S.M wrote the manuscript.

DECLARATION OF INTERESTS

The authors declare no competing interests.

FIGURE LEGENDS

Figure 1: **MCPH1 expression in RGCs in the developing nctx diverges between mouse and human**

(A-F) Mcph1 IF (red) on mouse nctx at E10.5 (A, B) and E12.5 (C-G), combined with (A-D) DAPI nuclear staining (blue) and with (D) γ-Tubulin (green; yellow stars indicate γ-Tubulin, not Mcph1, expression at centrosomes), (E) RC2 (green) and (F) Tbrce IF; right panel is a higher-magnification image of the area boxed in the right panel.

(G) Single plan sections extracted from 3D reconstructions of confocal Z-stack pictures obtained from whole-mount E12.5 nctx labeled with mouse monoclonal Mcph1 antibody (green) and (upper panel) Dock7 and Phalloidin Deep Red (respectively red and grey); (middle panel) Par3 (red); and (lower panel) APC (red). Yellow arrows indicate orientation from the apical (a) to the basal (b) side.

(H-L) MCPH1 (red) co-IF with (H, J) PAX6 (green), (K) SOX2 (green), (L) TBR2 (green), combined with (H) DAPI staining (blue) on the VZ/SVZ (left panels) and OSVZ (right panels) of a PCW11 human fetal cortex.

Bars, 50 μm in A, C, H-L; 20 μm in F; 10 μm in B, D and E;

See also Figure S1

Figure 2: **The conditional deletion of *Mcph1* induces micorcephaly in the mouse neocortex (nctx).**

A) Cresyl violet staining on p5 control (Ct) and *Mcph1* conditional knock out (cKO) nctx; black lines delineate the neocortical area, red lines indicate the neocortical radial thickness. Bar, 400 μm.

(B) Microcephaly in *Mcph1* cKO embryos is underlined by a decrease in the brain weight (Ct n=12; cKO n=9; $p<0.05$), in the neocortical surface (Ct n=4, cKO n=3; $p<0.01$), in both the lateral (Ct n=4, cKO n=4, $p<0.05$) and the radial (Ct n=4, cKO n=4 $p<0.01$) extent; Unpaired Student's *t* test; Error bars, SEM. Red and blue bars represent Ct and cKO, respectively.

(C) Birth date tracing of layer (L) neurons analyzed after BrdU injection at E14.5 by co-IF BrdU (red) and either Tbr1 (LVI), Ctip2 (LV), Satb2 (LIV-II) or Cux1 (LII-III), all green. Yellow lines delineate cortical layers; DAPI staining (blue) in upper left panels. Bar, 100 μm.

(D) Quantification of the total number of neurons in the cortical plate (DAPI-stained nuclei; Ct n=4, cKO n=3) and of the BrdU distribution in Tbr1+ (LVI; Ct n=3, cKO n=3); Citp2+ (LV; Ct n=3, cKO n=3); Satb2+ (LIV-II; Ct n=3, cKO n=3) or Cux1 (LIII-II; Ct n=4, cKO n=3) neurons, all green; *ns*, not statistically significant; *$p<0.05$; Unpaired Student's *t* tests; Error bars, SEM.

(E) DAPI-staining (blue) combined with phospho-Histone H3 (PH3, grey) and cleaved Caspase3 (CC3, green) double IF on E12.5 Ct and cKO nctx. Bar, 100 μm.

(F) DAPI-staining (blue) combined with CC3 (green) and Tbr2 (red) co-IF on E12.5 cKO nctx. Bars, left panel 20 μm, right panel 5 μm.

(G) Quantification of CC3 positive cells in Ct and cKO cortices at E11.5 (Ct n=4, cKO n=3; $p<0.05$), E12.5 (Ct n=3, cKO n=3; $p<0.001$), E14.5 (Ct n=3, cKO n=4; $p<0.01$) and E16.5 (Ct n=3, cKO n=3, $p<0.05$); *ns*, not statistically significant; Unpaired Student's *t* test; Error bars, SEM.

(H) Quantification of PH3 positive cells in the VZ (green bars) and SVZ (purple bars) of Ct (n=4) and cKO (n=4) nctx at 11.5, E12.5 ($p<0.05$), E14.5 and E16.5; *ns*, not statistically significant; Unpaired Student's *t* test; Error bars, SEM.

See also Figure S2

Figure 3: Mcph1 interacts with mitochondria and impacts the mitochondrial network.

(A) Gene enrichment tested using Gene set enrichment analysis (GSEA) for the Molecular Signature database (MSigDB) hallmark gene sets following transcriptome analysis from WTNPCs and KONPCs. The most significantly enriched ($p<10^{-4}$) pathways regulated negatively and positively are presented with green and orange bars, respectively.

(B) DAPI (blue) and MitoTracker Deep Red (MitoT, grey) staining combined with Mcph1 (red) and SDHA (green) co-IF on WTNPCs; lower panels, higher magnification images of the area boxed in the upper panels. Bars, 10 μm upper panels, 3 μm lower panels.

(C) Mcph1 gold immunostaining on E12.5 mouse nctx analyzed by electronic microscopy pointed by black arrows; n, nucleus. Bar, 5 nm.

(D) DAPI (blue) and MitoT (grey) staining combined with GFP (green) and HA (red) co-IF in WTNPCs transiently transfected with pCAGG-MCPH1-HA-IRES-GFP.

(E) DAPI (blue) and MitoT staining (grey) combined with MCPH1 IF (red) in human NPCs (hNPCs).

(F) DAPI (blue) and MitoT (grey) staining combined with SDHA (green) IF in WTNPCs and KONPCs.

(G) Quantification of the mitochondrial respiratory chain complex I by ELISA in WTNPCs (red bars, n=7) and KONPCs (blue bars, n=6); *ns*, not statistically significant; Error bars, SEM; Unpaired Student's *t* test.

(H) Comparison of VDAC1 expression in WTNPCs (red bars; n=3) and KONPCs (blue bars; n=3) by Western blotting; *ns*, not statistically significant; error bars, SEM; Unpaired Student's *t* test.

(I) Electron microscopy comparative analysis of the mitochondrial network (black arrows) in WTNPCs and KONPCs and quantification of the mitochondria mean surface (*ns*, not statistically significant), total number ($p<0.01$) and mean parameter ($p<0.05$) between WTNPCs (red bars) and KONPCs (blue bars). Data represent the mean of 3 independent experiments including 6 cells of each genotype; Non-parametric Mann-Whitney U test; Error bars, SEM.

Bars, 10 µm in C, D, E and 20 µm in F, 500 nm in I

See also Table S1

Figure 4: The *Mcph1* mutation alters mitochondrial functionality

(A-F) Activity of the various segments of the respiratory chain in WTNPCs and KONPCs maintained in GPGln (purple signs), PGln (red signs) and Gln (blue signs) medium: (A), Malonate-sensitive succinate reductase (SCCR, CII+CIII); (B) Glycerol cytochrome *c* reductase (GCCR, G3PDH+CIII); (C) Decylubiquinol cytochrome *c* reductase (QCCR, CIII); (D) Cyanide-sensitive cytochrome c oxidase (Cox, CIV); (E) Rotenone-sensitive NADH quinone reductase (CI); (F) Oligomycine-sensitive ATPase (CV). Enzymatic activities were measured in two separate sets of experiments, each including a group of NPCs in GPGln (control) and a second group of NPCs maintained either in PGln or in Gln medium. For statistical analyses, the values obtained in the control GPGln condition from the two sets

were pooled (WTNPCs n=14 for all enzymes except for ATPase, n=10; KONPCs n=14 and 10, respectively); in PGln medium, n=4 for WTNPCs and n=5 for KONPCs for all enzyme, except for ATPase, n=3 and n=5 respectively; in Gln medium, samples of WTNPCs and KONPCs correspond, respectively, to n=8 and n=6 for SCCR, GCCR and Cox, n=8 and n=10, for ATPase, n=8 in each group for NADH reductase. *ns*, not statistically significant; **p*<0.05, ***p*<0.001; One way ANOVA Tukey-Kramer multiple comparison test; Error bars, SD.

(G) Transient expression of the fluorescent mitochondrial calcium reporter protein mito-GEM-GECO1 in WTNPCs and KONPCs. Signal of the protein free of Ca2+ (- Ca2+) and bound to Ca2+ (+Ca2+) is illustrated in red and blue, respectively. Bar, 10 µm.

(H) Heat map indicates the fluorescence scale ratio. Quantification of fluorescence ratios in WTNPCs (n=24 cells) and KONPCs (n=30 cells) maintained in PGln and from 3 different experiments; *p*<0.001; Two tailed Mann-Whitney U-test; Error bars, SEM.

(I) Quantification of cell death in WTNPCs (purple signs; n=4) and KONPCs (orange signs; n=4) maintained in GPLN, PGln and Gln medium. Total cells (DAPI stained nuclei) and cells expressing cleaved caspase-3 were counted on 5 images per sample. Data are reported as percentage of cleaved caspase-3 positive cells. *ns*, non statistically significant; **p*<0.05; ***p*<0.01; ****p*<0.001; One way Anova Tukey-Kramer Multiple Comparison Test; Error bars, SEM.

(J) Hexokinase I-IV (HK) and (K) Lactate dehydrogenase (LDH) activities measured in protein extracts of WTNPCs (n=4) and KONPCs (n=3) maintained in GPGln (black signs), PGln (red signs) or Gln medium (blue signs). *p*<0.01; *ns*, not statistically significant; one way ANOVA Tukey-Kramer Multiple Comparison Test; Error bars, SD.

See also Figure S3

Figure 5: Mcph1 controls the ATF4/PCK2 pathway in mouse NPCs.

(A) DAPI-staining (blue) and PCK2 IF on WTNPCs. Bar, 10 µm.

(B) Western blot analysis of PCK2 expression in WTNPCs and KONPCs in GPGln, PGln or Gln medium (n=3; $p<0.01$); expression level in KONPCs was too low for quantification; *ns*, not statistically significant; One way ANOVA Tukey-Kramer Multiple Comparison Test; Error bars, SEM.

(C) DAPI-staining (blue) and PCK2 IF (red) on E10.5 WT (upper panels) and KO (lower panels) mouse nctx. Confocal pictures were monitored with identical laser setting. Bar, 20 µm.

(D) Tile-scan of an E12.5 WT mouse nctx section immunostained for PCK2 and illustrating ventro-dorsally increasing PCK2 expression. Bar, 100 µm.

(E) DAPI-staining (blue) and PCK2 IF (red) on E14.5 WT nctx. Bar, 50 µm.

(F) Western blot analysis of ATF4 expression in WTNPCs and KONPCs in GPGln, PGln or Gln medium (n=3 for each group); expression level in KONPCs was too low for quantification; *ns*, not statistically significant; *$p<0.05$; **$p<0.01$; ***$p<0.001$); One way ANOVA Tukey-Kramer Multiple Comparison Test; Error bars, SEM.

(G) Western blot analysis of GRP78 expression in WTNPCs (n=6) and KONPCs (n=5) in GPGln, PGln or Gln medium; *ns*, not statistically significant; One way ANOVA Tukey-Kramer Multiple Comparison Test; Error bars, SEM.

See also Figure S4

Figure 6: Comparative effects of 2-DG, alone or coupled to BPTES or UK5099, on the proliferation of WTNPCs and KONPCs

(A) Dot plots of EdU and PI signal analysis by flow cytometry in representative WTNPC and KONPC samples, non-treated control (Ct) or upon 2-DG, 2-DG+BPTES and 2-DG+UK5099 exposure. The cell distribution in the cell cycle phases « G0/G1 », « S », and « G2/M » is expressed in percentages.

(B) Quantitative analysis of the effects of metabolic inhibitors on the proliferation of WTNPCs (red signs) and KONPCs (blue signs). Ct, control untreated cells; 2DG (2-DG); 2DG+B (2-DG+BPTES) and 2DG+U (2DG+UK5099). The distribution of cells in G0/G1 (B), S (C) and G2/M (D) phase is expressed as percentages relative to the control condition; *ns*, not statistically significant; *$p<0,05$,

**p<0,01, ***p<0,001; One way Anova Tukey-Kramer Multiple Comparison Test; Error bars, SD.

See also Figure S5

Figure 7: MCPH1 interacts with the VDAC1/GRP75 pathway

(A) Co-immunoprecipitation (Co-IP) of GRP75-FLAG and HA-MCPH1 proteins, full length or deleted of BRCT domains (BR1, N-terminal; BR2 and BR3, C-terminal; Δ, deletion) co-expressed in HEK293T cells; Left panel, input for each protein, 10% of the protein amount used for Co-IP; Right panel, Co-IP with FLAG antibodies followed by immunoblotting (IB) with HA and FLAG antibodies.

(B) Western blot quantification of GRP75 expression in WTNPCs (n=6; red bars) and KONPCs (n=5, blue bars); p<0.05; Unpaired Student's t test; Error bars, SEM.

(C) DAPI-staining (blue) and Proximity Ligation Assay (PLA, red dots) on WTNPCs (WT) in GPGln, PGln or Gln medium performed with Mcph1 antibodies coupled to either GRP75 (upper panel) or VDAC1 (lower panels) antibodies.

(D) For each group, dot count was collected on an average of 30 cells from 3 independent experiments; *ns*, not statistically significant; *p<0.05; **p<0.01, ***p<0.001; One way ANOVA non-parametric Kruskal-Wallis test followed by Dunn's Multiple; Error bars, SEM.

(E) DAPI-staining (blue) and PLA (red dots) performed on human NPCs (hNPCs) in GPGln, PGln or Gln medium by coupling MCPH1 antibodies to either GRP75 (upper panels) or VDAC1 (lower panels) antibodies.

(F) Dot counts grouped from two independent experiments on two individual hNPC primary cultures; *ns*, not statistically significant; *p<0.05; One way ANOVA non-parametric Kruskal-Wallis test followed by Dunn's Multiple; Error bars, SEM.

(G) DAPI-staining (blue) and PLA (red) with VDAC1 and GRP75 antibodies on WTNPCs and KONPCs. The data were validated in 5 individual cultures of WTNPCs and KONPCs in two distinct experiments.

(H) DAPI-staining (blue) and PLA (red) on E10.5 mouse nctx with Mcph1 antibodies coupled to VDAC1 (left panels) or GRP75 (right panels) antibodies; lower-panels, higher magnification images of white boxes.

Bars, 10 μm in C, E, G; 20 μm in H upper panels and 10 μm in H lower panels.

See also Figure S6

STAR METHODS

Detailed methods are provided in the online version of this paper and include the following:

- **KEY RESSOURCES TABLE**
- **LEAD CONTACT AND MATERIALS AVAILABILITY**
- **EXPERIMENTAL MODEL AND SUBJECTS DETAILS**
  - Mouse lines
  - Human tissues
- **METHODS DETAILS**
  - Tissue processing
  - Embryonic neuroprogenitor cell (NPC) primary culture
  - Immunofluorescence
  - *In situ* hybridization
  - Imaging and cell counts
  - Electron microscopy
  - Proximity Ligation Assay (PLA)
  - Ca^{2+} imaging and quantification
  - Western blotting and ELISA
  - FACS analyses
  - Plasmids and transient transfections
  - Co-Immnunoprecipitations
  - Mitochondrial respiratory chain and metabolic enzymes activities
  - Sample preparation for RNA-seq analysis
  - Gene expression analysis in mouse NPCs
  - Analysis of MCPH1 expression in transcriptomic data from the Human BrainSpan Atlas
- **QUANTIFICATION AND STATISTICAL ANALYSIS**
- **DATA AND CODE AVAILABILITY**

SUPPLEMENTAL INFORMATION

Supplementary Table S1 related to Figure 3: Enrichment for differentially expressed genes in *Mcph1* KO mouse versus wild type NPCs for several sets of genes.

KEY RESOURCES TABLE

REAGENT or RESOURCE	SOURCE	IDENTIFIER
Antibodies		
MCPH1 (rabbit)	Abcam	Cat # ab2612
MCPH1 mouse exon 8, aa221-598 (rabbit)	Proteintech Group Inc customer service	N/A
MCPH1 mouse exon 9-14 aa600-822 (rabbit)	Proteintech Group Inc customer service	N/A
MCPH1 (mouse)	Abgent	Cat# AT2823a
Vimentin phospho S55 (mouse)	Abcam	Cat # ab22651 RRID AB_447222
gamma Tubulin (mouse)	Abcam	Cat # ab27074 RRID AB_2211240
SATB2 (mouse)	Abcam	Cat # ab51502 RRID AB_822455
Tpx2 (rabbit)	Santa Cruz	Cat # sc-32683
SDHA (rabbit)	Abcam	Cat # ab14715 RRID AB_301433
VDAC1 (mouse)	Abcam	Cat # ab14734 RRID AB_443084
VDAC1 (rabbit)	Abcam	Cat # ab15895 RRID AB_2214787
HSPA9/GRP75 (mouse)	Santa Cruz Biotechnology	Cat # sc-133137 RRID AB_2120468
HSPA5/GRP78 (mouse)	Millipore	Cat # MAB C675 RRID
Pax6 (mouse)	DSHB	PAX6 RRID AB_528427
TBR2 (rabbit)	Abcam	Cat # ab15894 RRID AB_10615604
TBR2 (chick)	Millipore	Cat # AB15894 RRID AB_10615604
Tbr2 (rat)	eBioscience	Cat # 14-4875-82 RRID AB_11042577
TBR1 (rabbit)	Abcam	Cat # ab31940 RRID AB_2200219
Cux1 (rabbit)	Santa Cruz Biotechnology	Cat # sc-13024
cleaved Caspase 3 (rabbit)	Cell Signalling	Cat # 9664 RRID AB_2070042
Par3 (rabbit)	Millipore	Cat # 07-330 RRID AB_11213581
APC (rabbit)	Santa Cruz Biotechnology	Cat # sc-896
PCK2 (rabbit)	Cell Signalling	Cat # 6924
HA (rat)	Roche	Cat # 11867423 RRID AB_2314621
CTIP2 (rat)	Abcam	Cat # ab18465 RRID AB_2064130
Phospho-Histone H3 (rat)	Abcam	Cat # ab10543 RRID AB_2295065
BrdU (rat)	Abcam	Cat # ab6326 RRID AB_305426
DOCK7 (goat)	Santa Cruz Biotechnology	Cat # sc-104220 RRID
HK2 (goat)	Santa Cruz Biotechnology	Cat # sc-6521
GFP (chick)	Aves	Cat # GFP-1020 RRID AB_10000240
AKT total (rabbit)	Cell Signalling	Cat # 4691 RRID AB_915783
pAKT S473 (mouse)	Cell Signalling	Cat # 4051 RRID AB_331158
pAKT T308 (mouse)	Santa Cruz Biotechnology	Cat # sc-271966 RRID AB_10715102

PDPK1 (rabbit)	Abcam	Cat # ab109253
ATF4 (rabbit)	Cell Signalling	Cat # 11815 RRID AB_2616025
Beta-Actin (mouse)	Millipore	Cat # MABT826
FLAG M2 (mouse)	Sigma-Aldrich	Cat # F1804 RRID AB_262044
Nanogold®-conjugated goat anti rabbit IgG	Nanoprobes	Cat # 2001-1 mL
Biological Samples		
Human tissues	Gynecology-Obstetric Department at Robert Debre Hospital, Paris	N/A
Chemicals, Peptides, and Recombinant Proteins		
UK-5099	SSIGMA Aldrich	Cat # PZ0160
BPTES	SIGMA Aldrich	Cat # SML0601
2-Deoxyglucose	SIGMA Aldrich	
MitoTracker Deep Red	Invitrogen	Cat # M7514
Phalloidin	Invitrogen	Cat # A22284
Phosphatase and protease cocktail inhibitor	Thermofisher	Cat # 815-968-0747
Fluoromount-G mounting medium	SouthernBiotech	Cat #0 Cat # 100-01
DAPI (4', 6-diamidino-2-phenylindole)	Sigma Aldrich	Cat # D9542
Entellan	Millipore	Cat #107961
Durcupan ACM	Fluka	Cat # 44610
Protease inhibitor	Roche	Cat # 04693159001
Critical Commercial Assays		
DUOLINK kit	SIGMA Aldrich	Cat # DUO92101
ELISA Complex I Rodent profiling kit	Abcam	Cat # ab136809
HA-Tag Magnetic Co-IP kit	Pierce	Cat # 88838
CellROX® Deep Red Flow Cytometry Assay Kit	Invitrogen	Cat # C10493
647 EdU Click Proliferation Kit	Invitrogen.	Cat # C10491
Cy3 TSA amplification kit	BD Biosciences	Cat # 565456
QIAquick PCR purification Kit	Perkin Elmer	Cat # SAT704A001EA
Sybr Green Supermix	Bio-Rad	Cat #1708880
Quickchange XL Site-Directed Mutagenesis Kit	Qiagen	Cat # 28104
ScriptSeq V2 kit	Stratagene/Agilent Technologies	Cat # 200516
Ribo-Zero kit	Epicentre	Cat # SSV21106, #SSV21124
ExGen500	Epicentre	Cat # MRZH11124, #MRZH116
RNeasy Mini Kit	Euromedex	Cat # R0511
iScript cDNA Synthesis Kit	Qiagen	Cat # 74104, #2012
Deposited Data		
WT and Mcph1 KO NPC Transcriptomes	GSE140976	
Mouse FAST DB	omicX	V2013,1
Molecular Signatures Database		V5.2
Experimental Models: Cell Lines		
HEK293T	ATCC	CRL-11268
Experimental Models: Organisms/Strains		

Mouse*: B6.129S2-Emx1tm1(cre)Krj/J (Emx1$^{Kicre/+}$)*	The Jackson Laboratory	Emx1- kiIRES cre
Mouse: Mcph1$^{tm1a(EUCOMM)Wtsi}$	EUCOMM	244329
Mouse*: B6;SJL-Tg(ACTFLPe)9205Dym/J (beta-Actin-FLP)*	The Jackson Laboratory	ACTB:FLPe B6;SJL
Mouse*: Mcph1 lox/+; Emx1kicre/+*	This paper	N/A
Mouse：Mcph1$^{tm1.2Kali}$	Liang et al., PLos Genetics, 2010, 6(1)e1000826	N/A
Mouse: C57BL/6J	Charles River	C57BL/6J
Oligonucleotides		
m*ATF4*-F: 5'CCTATAAAGGCTTGCGCCCA3'	This paper	N/A
m*ATF4*-R: 5'GCTGGATTTCCTGAACAGCG3'	This paper	N/A
m*PCK2*-F: 5'TGTCACCATAACCTCGTGCT3'	This paper	N/A
m*PCK2*-R: 5'TAGGGACACCTTCTGGTGCT3'	This paper	N/A
m*GLS1*-F: 5'AGGCAGTTCGGAATACACTGA3'	This paper	N/A
m*GLS1*-R: 5'AAGAATACCCCCAGCAACTCC3'	This paper	N/A
m*GLUD1*-R: 5'CTACGGCCGATTGACCTTCA3'	This paper	N/A
m*GLUD1*-R: 5'GCACCCGATATCCTGTCCTG3'	This paper	N/A
mRpl13a-F : 5'ACA GCC ACT CTG GAG GAG AA3'	This paper	N/A
mRpl13a-R 5'GAG TCC GTT GGT CTT GAG GA3'	This paper	N/A
Recombinant DNA		
Mouse *Mcph1* cDNA	IMAGE	#5697978
pCAGGS-MCPH1FL-HA	This paper	N/A
pCAGGS-MCPH1ΔBR2/3-HA	This paper	N/A
pCAGGS-ires-EGFP	Magnus et al Science. 2011 Sep 2;333(6047):1292-6.	Addgene #32482
pCMV-mito-GEM-GECO1	Zhao et al Science. 2011 Sep 8.	Addgene #32461

pcDNA3-MCPH1 full-length, Δ□□1, ΔBR2, ΔBR2-3	This paper	N/A
pcDNA3-GRP75	This paper	N/A
Software and Algorithms		
FIJI/ImageJ	Schneider et al., 2012	https://imagej.nih.gov/ij/
Photoshop C3 Adobe Systems		https://www.adobe.com/products/photoshop.html
Excel	Microsoft	https://products.office.com
GENEsys V1.5.4.0 software	Syngene	V1.5.4.0
STAR (v2.3.0)	Dobin et al., 2013	http://code.google.com/p/rna-star/.
FastQC	Babraham Bioinformatics	V0.10.1
Rseqc	Github	V2.4
Picard-Tools	Broad Institute	V1.119
Samtools	Source Forge. Github	V0.1.19
Primer3 plus Software	Primer3	http://primer3plus.com
Morada Soft Imaging System	Olympus Soft Imaging Solutions	www.soft-imaging.net
GraphPadPrism 5.0 software	GraphPad Prism Software Inc.	https://www.graphpad.com/scientific-software/prism/
And Deseq	Bioconductor	V.1.12.1
Bio-Rad CFX Manager	Bio-Rad	3.0
BiomaRt Bioconductor R package	Naro et al., 2007; Noli et al., 2015	V2.40.4

LEAD CONTACT AND MATERIALS AVAILABILITY

Further information and requests for resources and reagents generated in this study should be directed to and will be fulfilled by the Lead Contact, Jeannette Nardelli (jeannette.nardelli@inserm.fr). All unique/stable reagents generated in this study are available from the Lead Contact with a completed Materials Transfer Agreement.

EXPERIMENTAL MODEL AND SUBJECTS DETAILS

Mouse lines.

All mouse lines were maintained in the C57Bl/6J genetic background. All animals were handled in strict accordance with good national animal practice as defined by the national rules, and all the mouse work was approved (# B75-19-01) by the Paris DDPP (Département De Protection des Populations).

The Emx1$^{tm1(cre)Krj}$/J (Jackson laboratory #005628) and the *Mcph1* $^{Mcph1<tm1.2Kali>}$ full knock out (KO) mouse lines were respectively described in Gorski et al., 2002 and in Liang et al., 2010. To generate *Mcph1* $^{lox/lox}$ control and *Mcph1*$^{lox/lox}$*; Emx1*$^{Kicre/+}$ conditional knock out (cKO) mice, *Mcph1* $^{lox/+}$ were derived from the Mcph1$^{tm1a\ (Eucomm)wtsi}$ mice after crossing with beta-Actin-FLP mice (Rodriguez et al., 2000) for excision of the lacZ-neo cassette, then crossed with the *Emx1*$^{kicre/+}$ mice to produce *Mcph1* $^{lox/+}$*; Emx1*$^{kicre/+}$ mice, which were finally mated with *Mcph1* $^{lox/lox}$ mice. The *Mcph1* mutation in the KO and the cKO mice consists in the deletion of exon2 or exon 4 respectively, leading to out of reading frame mutation of *Mcph1* in both cases. Midday of the vaginal plug observation was considered as embryonic day (E) 0.5. Pregnant females received intra-peritoneal BrdU injection (50 mg/kg) at relevant stages of gestation and sacrificed 1 hour after injection for proliferation studies at E12, E14.5 and 2h at E16.5, while pups were sacrificed at P0 or P5 for neuron tracing. Animals and embryos were genotyped by PCR on DNA extracted from tail and yolk salk, respectively.

Human tissues

All human tissues were obtained from the Gynecology-Obstetric Department at Robert Debre Hospital, Paris, according to the rules established by the French Bioethics Agency and with parental consent. 9-10 or 11 and 13 Post Conception Weeks (PCW) fetal brains were obtained after volunteer abortion or spontaneous pregnancy termination, respectively.

Cell lines

MCPH1 and GRP75 Expression was obtained in HEK293T cells by transient transfection.

METHODS DETAILS

Tissue processing

Whole E10.5 to E12.5 embryos were fixed in 4% paraformaldehyde (PFA, Sigma Aldrich), whereas E14.5 to P5 brains were dissected before fixation in the same solution. Tissues were cryo-protected in 30% sucrose in Phosphate buffered saline (PBS), embedded in gelatin before freezing and

kept at -80°C until use. Serial 12 micron-thick sections were cut on a Leica CM 3050 cryostat. Sections of P5 cortices were stained in a 0.3% cresyl violet solution, dehydrated and mounted in Entellan (Millipore) for brain morphometric analysis. For whole mount staining, fixed brains were rinsed in PBS and dorsal telencephalon was dissected before immunostaining.

After fixation in PFA, human fetal brains were processed as described for mouse brains.

Embryonic neocortical neuroprogenitor cell (NPC) primary culture.

Mouse dorsal telencephalon was dissected from E12.5 brains in DMEM/F12 medium (Invitrogen). Cell suspension was obtained by mechanical dissociation. NPCs from each telencephalon were grown individually as neurospheres in 6 well plates and in DMEM/F12 medium supplemented with 1xN2 and 0.5xB27, 10 ng/ml FGF (Invitrogen) and bFGF (Sigma Aldrich) and 10 µg/ml Insulin (Sigma Aldrich). Two days after the culture start, wild type (WTNPCs) or *Mcph1* KO (KONPCs) primary cultures were pooled by two or three in a T75 flask for further expansion during two to three days. At this stage, neurospheres were pelleted for protein or RNA extraction, or mechanically dissociated for seeding on gelatin-coated dishes, glass coverslips in 24-well plates or IBIDI slides (IBIDI). Attached cells were cultured in DMEM medium (Invitrogen) supplemented with 10% fetal bovine serum and either i) 4,5 g/L Glucose, 1mM sodium pyruvate and 1mM Glutamine (GPGln complete medium); ii) 2mM sodium pyruvate and 1mM Glutamine (PGln medium); iii) 1mM Glutamine only (Gln medium). Cells were then maintained in culture for four days.

For exposure to 2-DG (1mM), BPTES (1µM) or UK5099 (1µM), NPCs were primarily seeded in DMEM medium containing 1 g/L Glucose, 1mM sodium pyruvate and 1mM Glutamine for 24h. Inhibitors were added into the medium and cells left in contact with inhibitors for 24 hours.

Primary cultures of human embryonic neocortical NPCs (hNPCs) were generated from dorsal telencephalons dissected on embryos collected at 9-10 PCW by following the procedure afore-described for mouse NPCs.

Immunofluorescence

Two rabbit antibodies were raised against the mouse Mcph1 protein by the customer service of the Proteintech Group Inc. One antibody was raised to a synthetic internal polypeptide encoded by exon 8 (aa221-598), the second antibody to a synthetic peptide including the two C-ter BRCT domains encoded by exons 9-14 (aa600-822). The specificity of the two antibodies was established in transiently transfected NPCs expressing HA-tagged Mcph1 proteins, either complete or deleted of the two C-Ter BRCT domains. Both Mcph1 antibodies were diluted 1:2000 for immunofluorescence, to conduct expression studies from E10.5 to E16.5, along with a commercial mouse monoclonal MCPH1 antibody directed against the human MCPH1 protein (Abgent). The three antibodies produced matching results on not frozen tissues, such as whole mount cortices. On frozen sections, only our custom-made antibodies gave specific and matching results, but required the use of a Cy3 TSA amplification kit (Perkin Elmer). Unless specified the data presented here were obtained with the Mcph1-Cter antibodies. Human MCPH1 protein expression was detected using the same procedure and Abcam MCPH1 antibodies (ab2612).

Immunodetection of other molecular markers was performed as described (El Wakil et al., 2006). To follow with BrdU co-staining, immuno-stained sections were post-fixed in PFA 4%, treated with HCl 2N at room temperature for 30 mn, rinsed in PBS and processed for BrdU staining. Whole dorsal telencephalon samples were permeabilized in PBS 0.3% triton X100, then saturated in PBS containing 10% normal goat serum (NGS) and 0.1% triton (PBGT) for at least two hours. Samples were then incubated at 4°C with primary antibodies diluted in PBGT either overnight (E12.5) or for two days (E14.5). After several washes in PBT, tissues were incubated for 2 hours (E12.5) or overnight (E14.5) in secondary antibodies diluted in PBGT containing 1 µg/ml DAPI (SIGMA Aldrich), washed in PBT and flat-mounted in Fluoromount-G (SouthernBiotech), and sealed with Entellan (Millipore).

NPCs were fixed in 4% PFA, rinsed in PBS, permeabilized in PBT during 15 minutes, and saturated with PBS containing 10% NGS (PBG) for one hour. Before fixation, NPCs were eventually incubated with 200 nM MitoTracker Deep red (Invitrogen) for 30 minutes. Primary antibodies diluted in PBG were incubated overnight and rinsed in PBS. Secondary antibodies diluted in PBG containing

1 µg/ml DAPI (4',6-diamidino-2-phénylindole) were applied for 30 minutes at room temperature, washed in PBS and coverslips were mounted in Fluoromount-G (SouthernBiotech).

The commercial antibodies used in our studies were: as mouse antibodies, MCPH1 (1:1000, Abgent #2823a), phospho-Vimentin-S55 (1:1000, Abcam ab22651), γ-tubulin (1:2000, Abcam ab27074), Satb2 (1:500, Abcam ab51502), SDHA (1:500; Abcam ab14715), GRP75 (1:250; Santa-Cruz Biotechnology sc-133137), GRP78 (1:500, Millipore #MABC675), PAX6 (1:20, DSHB PAX6), as rabbit antibodies, MCPH1 (1:2000, Abcam ab2612), Tbr2 (1:250, Abcam ab15894), Tpx2 (1:500; Santa Cruz Biotechnology sc-32683), Tbr1 (1:500, Abcam ab31940), Cux1 (1:500, Santa Cruz Biotechnology sc-13024), cleaved Caspase3 (1:2000, Cell Signaling #9664), Par3 (1:1000, Millipore #07-330), APC (1:1000, Santa Cruz Biotechnology sc-896), PCK2 (1:1000, Cell Signaling #6924), as rat antibodies, HA (1:2000, Roche #11867423), Ctip2 (1:1000, Abcam ab18465), phospho-Histone H3 (1:2000; Abcam ab10543), anti BrdU (1:1000, ab6326), as goat antibodies Dock7 (1:100, Santa Cruz Biotechnology sc-104220), HK2 (1:500, Santa Cruz Biotechnology sc-6521), as chick antibodies, anti GFP (1:2000, Aves GFP-1020), anti TBR2 (1:500, Millipore #15891). Co-staining was eventually performed with Phalloidin Deep Red (1/1000) and MitoTracker Deep Red (Invitrogen). Secondary Goat or Donkey antibodies were coupled to Alexa488, Alexa633 (Invitrogen), or to Cy3, Cy5 (Jackson ImmunoResearch). All were used diluted 1:2000.

***In situ* hybridization**

To analyze *Mcph1* expression by *in situ* hybridization, a cDNA fragment including nucleotides +1 to + 850 of the coding sequence was amplified from the IMAGE clone # 5697978 by PCR with a reverse primer including the T3 promoter sequence. The PCR product was checked on agarose gel and purified using the QIAquick PCR purification kit (Qiagen). A digoxigenin anti-sense RNA probe was used to performed *in situ* hybridization on sections of E10.5, E12.5, E14.5 and E16.5 embryonic brains, as described in (El Wakil et al., 2006).

Imaging and cell counts

Imaging was performed using a Leica TCS SP8 confocal scanning system (Leica Microsystems) equipped with 405-nm Diode, 488-nm Ar, 561-nm DPSS and 633-nm HeNe lasers. Eight-bit digital images were collected in a sequential mode from a single optical plane using a 63x HC PL APO CS2 oil-immersion Leica objective (numerical aperture 1.40) for cell analyzes. For brain sections and whole mounts samples, a 20x and a 40x HC PL APO oil-immersion objectives were used to take single plan, tiles or Z-stack images in a sequential mode. Pictures with composite colors and the corresponding Tiff files were generated on ImageJ and further processed on Photoshop C3 for sizing and eventually for improving color contrast. 3D reconstructions were obtained from Z-stacks images taken within 40-90 □m from the ventricle surface using the Leica 3D software (Leica Microsystems). Single plan images were sequentially extracted at different levels to examine the distribution of marker expression.

At P5, morphometric analyses were performed on ImageJ (Schneider et al., 2012) on transverse cortical sections stained with cresyl violet and selected at the level of the somato-sensorial area. The cortical thickness was measured by drawing lines perpendicular to the ventricle surface and extending within the whole cortical wall. The lateral size of the neocortex was measured by drawing a curved line following the cortical surface, from the boundary with the cingulate cortex to the rhinal fissure. Four brains of each group, conditional knock out and control, 4 to 8 sections from each brain, were included in the studies.

Cells were counted on cortical transverse sections obtained with a x20 objective and 1024x1024 resolution and surface of 500 x 700 µm (P0) and 600 µm x 1400 µm (P5) (width x height) was delineated on tile-scan images from the cortical surface in the S1 cortical area and using ImageJ (Schindelin et al., 2012). Neurons and BrdU were counted with the ImageJ cell counter plugin in each layer as defined by their respective specific markers: Tbr1 for layer VI, Ctip2 for layer V, Satb2 for layers IV-II, and Cux1 for layer II-III. Five brains of each P0 group and three brains of each P5 group, control and *Mcph1* cKO, with 2 to 5 sections per brain, were used in the study.

BrdU and Tbr2 positive cells count was performed on images cropped to a width of 250 µm at E12.5 (3 brains for each genotype), 400 µm at 14.5 (4 brains for each genotype) and E16.5 (3 control and 4 cKO brains). Two to five sections of each brain were included in the study.

The number of PH3+ dividing cells at the ventricle border or in the SVZ of E11.5 (3 control and 4 cKO brains), E12.5 (4 brains of each group), E14.5 (3 control and 4 cKO brains) and E16.5 (4 control and 5 cKO brains) nctx was counted according to a ventricular length (µm) calculated on Image J.

Activated caspase-3 positive NPCs were counted manually on 184 µm x 184 µm (1024 x 1024 pixels) images taken with an x63 objective. The number of DAPI-stained nuclei per image was counted with the ImageJ cell counter plugin. Counts were obtained from 4 different cultures of WTNPCS and KONPCS processed in two independent experiments and from an average of 20 images per culture condition.

Electron microscopy

NPCs were fixed for 20 min with 37°C pre-warmed 4% PFA with 0.1% glutaraldehyde in 0.1M phosphate buffer (PB) containing 4% sucrose. After washing in PB, cells were post-fixed post-fixed in 1% glutaraldehyde in PBS for 10 min at RT. And washing in PB, they were post-fixed in 1% osmium tetroxide in Phosphate buffer (PB) for 10 min at RT, washed in PB, and dehydrated in an ascending series of ethanol, which included 1% uranyl acetate in 70% ethanol. Cultures were then embedded in Durcupan ACM (Fluka) resin. After polymerization at 60°C for 48 h, coverslips were separated from the embedded cells, and resin blocks were processed for ultrathin sectioning on a Reichert Ultracut S microtome.

For preembedding immunocytochemical detection of Mcph1 at the ultra-structural level, the brains of the E12.5 embryos were quickly dissected and fixed in 4% PFA for at least 24 h at 4°C. Horizontal sections were cut on a vibratome at 70 µm and collected in PBS, equilibrated in 25% sucrose and 10% glycerol in 0.05 M PB, frozen rapidly in iso-pentane cooled in liquid nitrogen, and thawed in PBS at RT. Sections were pre-incubated for 30 min in 5% NGS in PBS, and were then

incubated overnight at RT in rabbit anti-Mcph1 antibody (1:1000) diluted in PBS containing 1% NGS. After washing in PBS, sections were incubated for 120 min in Nanogold®-conjugated goat anti rabbit IgG (1:100; Nanoprobes) diluted in PBS containing 2% of bovine serum albumin-c and 0.2% of cold water fish gelatin. Sections were washed in PBS and post-fixed in 1% glutaraldehyde in PBS for 10 min. After washings in PBS and 0.1 M sodium acetate buffer, pH 7.0, Mcph1 immuno-gold labeling was intensified using a silver enhancement kit (HQ Silver; Nanoprobes) for 5-10 min in the dark at RT. After washings in acetate buffer and in PB, sections were post-fixed in 1% osmium tetroxide in PB for 10 min at RT. After washings in PB, they were dehydrated in an ascending series of ethanol, which included 1% uranyl acetate in 70% ethanol. Sections were then treated with propylene oxide twice for 10 min, equilibrated overnight in Durcupan ACM (Fluka), mounted on glass slides and cured at 60°C for 48 h. Areas of interest including the dorsal telencephalon were cut out from the slides and glued to blank cylinders of resin. Blocks were cut in semithin sections (1 µm) and then in ultrathin sections on a Reichert Ultracut S microtome.

For both NPCs and sections of the dorsal telencephalon, ultrathin sections were collected on pioloform-coated single-slot grids, stained with lead citrate and examined with a Philips CM120 electron microscope equipped with Morada Soft Imaging System (Olympus Soft Imaging Solutions). The acquired images were equally adjusted for brightness and contrast, and composite illustrations were built in Adobe Photoshop CS3 (Adobe Systems).

Mitochondrial profiles in NPCs were identified and morphologically characterized using the Measure command of FIJI/ImageJ software (Schindelin et al., 2012; Schneider et al., 2012). Results were expressed as number of mitochondial profiles per μm^2 cytoplasmic surface and relative mitochondial surface compared to cytoplasmic surface. An average of 6 cells/group was analyzed in 3 independent experiments.

Proximity Ligation assay (PLA)

Proximity Ligation assays (PLA) were performed on NPCs seeded on glass-cover slips or E10.5 mouse cortical sections, formerly processed as for immunostaining. The assays were performed using a DUOLINK kit (SIGMA Aldrich), following the supplier instructions and with the following

antibody associations: rabbit Mcph1 C-ter/mouse GRP75 (1:250; Santa-Cruz sc-133137), rabbit Mcph1 C-ter/mouse VDAC1 (Abcam ab14734), mouse GRP75 (1:250; Santa-Cruz sc-133137)/rabbit VDAC1 (1/500, Abcam ab15895), goat HK2 (1/500; Santa Cruz Biotechonology)/rabbit VDAC1 (1/500).

Duolink signal was analyzed using a Leica TCS SP8 confocal scanning system (Leica Microsystems) and a 63x HC PL APO CS2 oil-immersion Leica objective (numerical aperture 1.40), as described before. Duolink particles and DAPI-stained nuclei were segmented and counted using the FIJI/ImageJ software (Schindelin et al., 2012; Schneider et al., 2012). Results were expressed as Duolink particles per nuclei and per 1000 μm^2 cytoplasmic surface. An average of 30 cells/group was analyzed in 3 independent experiments. Two sets of experiments, Duolink of Mcph1 and GRP75 and Duolink of Mcph1 and VDAC1 were analyzed, each set including 3 groups of cells: GPGln, PGln and Gln.

Ca^{2+} imaging and quantification

For ratiometric mito-GEM-GECO1 imaging of neuroepithelial cultures, the 405-nm Diode laser of a Leica TCS SP8 confocal scanning system (Leica Microsystems) was used. Emission windows were set to 427-467 nm (blue channel) and 502-537 nm (green channel). Eight-bit digital images were collected from a single optical plane using a 63x HC PL APO CS2 oil-immersion Leica objective (numerical aperture 1.40). Settings for laser intensity, pinhole (1 Airy unit), range property of emission window, electronic zoom, gain and offset of photomultiplicator, field format, scanning speed were optimized initially and held constant throughout the study so that all cells were digitized under the same conditions. Mitochondrial signals of the blue and green channels were segmented; their ratio was calculated and measured using the Analyze Particles command of FIJI/ImageJ (Schindelin et al., 2012; Schneider et al., 2012). An average of 26 cells/group, two groups corresponding to WT (n=3) and *Mcph1* KO (n=3) NPCs in PGln medium, was analyzed in 2 independent experiments. Mean ratio values for the experimental groups were calculated and statistically analyzed using the non-parametric Mann-Whitney U test.

Western blotting and ELISA

Pellets of NPCs cultured in GPGln, PGln or Gln medium were homogenized in RIPA buffer (SIGMA) with phosphatase and protease inhibitor cocktails (Invitrogen) added. Protein concentration was measured by the BCA method and using the Paradigm spectrophotometer (Beckman). Proteins were separated on Mini-Protean TGX 4-15% gels (Bio-Rad), transferred to PVDF membranes with a Trans-Blot TurboTransfert apparatus (Bio-Rad), then immunoblotted for VDAC1 (1:1000, Rabbit Abcam ab15895), GRP75 (1:1000, Mouse Santa Cruz Biotechnology sc-133137), HK2 (1:1000, Goat Santa Cruz Biotechnology sc-6521), PCK2 (1:1000, Rabbit Cell Signaling #6924), AKT total (1:1000, Rabbit Cell Signaling #4691), pAKT S473 (1 :200, Mouse Cell Signalling #4051), pAKT T308 (1 :200, Mouse Santa Cruz Biotechnology sc-271966), PDPK1 (1 :1000, Rabbit Abcam ab109253), ATF4 (1 :500, Rabbit Cell Signaling #11815), HA epitope (1 :1000, Rat Roche #11867423) and beta-Actin (1:20000, Mouse Millipore MABT826) as loading control. HRP conjugated secondary antibodies (Jackson Immunoresearch) were used diluted 1:20000 and bands were detected using the PXi multi-application image analysis system with the GENEsys V1.5.4.0 software (Syngene) and densitometry analysis on each blot was calculated using GENEsys-Tool (Syngene) or FIJI/ImageJ softwares. Densitometry values were normalized to beta-Actin. For each protein, the normalized expression ratio was established for each analyzed sample by calculating the marker/Actin densitometric ratio and dividing this ratio by the mean of the ratios obtained from the WT/GPGln control group. For quantification of phosphorylated Akt proteins, each ratio was normalized to the mean ratio obtained for total Akt in WTNPCs.

Mitochondria quantification was performed using the ELISA Complex I Rodent profiling kit (Abcam, ab136809), and following the supplier instructions. Optical densities were read at 450 nm using the Paradigm spectrophotometer (Beckman). Six *Mcph1* KO and 7 WT samples were included in the experiments.

FACS analyzes

Intracellular radical oxygen species (ROS) production and cell mortality were analyzed by

flow cytometry with the CellROX® Deep Red Flow Cytometry Assay Kit (Invitrogen, Thermo Fisher Scientific, Eugene, OR, USA). Cells were incubated with or without 400µM Tert-butyl hydroperoxyde (TBHP) for 2 hours, and with 1000nM CellRox and 1µM SYTOX respectively for the last 60 and 15 minutes. After trypsinization, cells were analyzed by flow cytometry. The gating strategy selected FSC and SSC singlets, with exclusion of $SYTOX^{high}$ apoptotic cells.

Cell cycle was analyzed by EdU incorporation and DNA content measurement using 647 EdU Click Proliferation Kit (BD Biosciences) and propidium iodide (PI), respectively. EdU was added to cell cultures during the last 3 hours of incubation with metabolic inhibitors. After trypsinization, click reaction and PI staining were performed according to manufacturer recommendations. Cells were analyzed by flow cytometry. The gating strategy selected FSC and SSC singlets, followed by selection of cells in "G0/G1", "S" and "G2/M" phases. For each cell cycle phase results were expressed as percentage relative to control condition.

Plasmids and cell transient transfections

For transient expression in NPCs cells, the human full-length (FL) *MCPH1* cDNA was synthesized with the HA-tag sequence fused at the 3' end, and subcloned into the Xho/XbaI restriction sites of the pCAGGS-IRES-GFP (Addgene # 32482) plasmid by the customer service of the GenScript Biotech Corporation to generate the pCAGGS-MCPH1FL-HA. To produce the pCAGGS-MCPH1ΔBR2-3-HA, the sequence overlapping exons 1 to 8 was amplified by PCR, sub-cloned into the same plasmid using the same strategy and checked by sequencing. pCMV-mito-GEM-GECO1 was a gift from Robert Campbell (Addgene plasmid #32461). Transient transfections were performed in NPCs using ExGen500 (5 µl per 1 µg of DNA and per well of a 24 well plate; Euromedex). NPCs were seeded either on glass coverslips for immunostaining or IBIDI chambers (IBIDI) for live imaging, and cells analyzed 24 hours after transfection. For live imaging, NPCs were placed in HBSS containing 15 mM HEPES, kept in a chamber à 37°C, and imaging was performed as described previously. For MCPH1 and GRP75 co-immunoprecipitation (co-IP), human full-length *MCPH1*

cDNA were obtained from HeLa mRNA and cloned into pcDNA-3HA vector using EcoRI/XhoI sites. *MCPH1* mutants (ΔBR1: 94-835aa, ΔBR2: Δ671-730aa, ΔBR3: 1-730aa, ΔBR2-3: 1-670aa) were produced using a Quickchange XL Site-Directed Mutagenesis Kit (Stratagene). Human *GRP75* cDNA was cloned into pcDNA-3FLAG vector using XhoI sites. The transfection of HEK293T cells was performed with polyethylenimine (PEI, Polyscience, Eppelheim, Germany) at a ratio of 5µg HA-MCPH1-FL or mutants plasmids and 5 µg FLAG-GRP75 in 30 µg PEI solutions. Co-IP was performed 48hr after transfection. For MCPH1 and VDAC1 Co-IP, the pCAGGS-ires-GFP MCPH1-HA constructs afore described were transfected in HEK293T cells using the same conditions than for NPCs.

Co-immunoprecipitations

For MCPH1 and GRP75 Co-IP, cell pellets were incubated in NETN lysis buffer (50mM Tris-HCl [pH 7.5], 150 mM NaCl, 5 mM EDTA, 0.5%NP-40, and protease inhibitor cocktail (Roche, #04693159001) on ice for 30 min. For IP, 2 µg of the anti-FLAG antibody (Sigma-Aldrich, F-1804) were incubated with 1mg of total lysate together with the protein G SepharoseTM 4 fast flow (GE Healthcare) at 4°C overnight. The precipitates were washed with the NETN buffer without protease inhibitors. MCPH1 and VDAC1 Co-IP were performed using the Perkin-Elmer HA magnetic beads, following manufacturer instruction for cell extraction and Co-IP.

Mitochondrial respiratory chain and metabolic enzymes activities

Cells were scraped in cold PBS, quickly pelleted at 4°C and kept frozen at -80°C until use. The activity of the various complexes of the mitochondrial respiratory chain and of Glucose-6-Phosphate Dehydrogenase (G6PDH), total hexokinase (Hexo I-IV), lactate dehydrogenase (LDH), NADP- dependant Isocytrate dehydrogenase (IDH1-2) and NAD+ dependant isocitrate dehydrogenase (IDH 3) activities were monitored on cell pellets, at 37°c and by spectro-photometry (double wavelength spectrophotometer (Cary 60, Varian, or Cary 50 spectrophotometer, Agilent Technologies, respectively) according to (Benit et al., 2006; Rustin et al., 1994). Protein content of cell pellets was estimated by the Bradford assay.

Sample preparation for RNA-seq analysis

Total RNA was extracted from NPCs obtained from WTNPCs and WTNPCs. Sample quality and quantification were assessed on Experion chips (Bio-Rad). Twin samples were pooled according to genotype and matching amounts. Library preparation and Illumina sequencing were performed on wild type and *Mcph1* KO samples, two of each, at the Genomic Platform of the Ecole Normale Superieure (Paris, France). Ribosomal RNA depletion was performed with the Ribo-Zero kit (Epicentre), using 1.5 µg of total RNA. Libraries were prepared using the strand specific RNA-Seq library preparation ScriptSeq V2 kit (Epicentre). Libraries were multiplexed by 4 on 1 flow cell lane. A 75bp read sequencing was performed on a HiSeq 1500 device (Illumina). A mean of 39.3 ± 7 million passing Illumina quality filter reads was obtained for each of the 4 samples.

Gene expression analysis in mouse NPCs

RNA-Seq data analysis was performed by GenoSplice technology (www.genosplice.com). Sequencing, data quality, reads repartition (e.g., for potential ribosomal contamination), and insert size estimation were performed using FastQC (v0.10.1), Picard-Tools (v1.119), Samtools (v0.1.19) and rseqc (v2.4). Reads were mapped using STAR (v2.3.0) (Dobin et al., 2013). Gene expression was estimated as already described (Dobin et al., 2013; Naro et al., 2017) using Mouse FAST DB v2013_1 annotations. Only genes expressed in at least Mutated Mcph1 cortex or WT cortex were further analyzed. Genes were considered as expressed if their rpkm value was greater than 97.5% of the background rpkm value based on intergenic regions. Raw count data normalization and differential expression analysis were then performed using Deseq (v1.12.1). Results were considered statistically significant for unadjusted p-values ≤ 0.05 and fold-changes ≥ 1.5.

The mouse dataset was annotated with human Ensembl gene ID using BiomaRt Bioconductor R package (Naro et al., 2017; Noli et al., 2015) and selecting human genes that were 'one-to-one' orthologues with mouse genes. As previously described (Delahaye-Duriez et al., 2016), we generated a gene-level score reflecting the significance and the intensity of differential expression (multiplying

the –log10 of p value by the log-transformed fold change). This score was used as a metric to 'rank' genes to test using Gene set enrichment analysis (GSEA) if gene sets defined in the Molecular Signatures database (MSigDB v5.2) occupy higher (or lower) positions in the ranked gene list than what it would be expected by chance (Subramanian et al., 2005). The enrichment was tested for several sets of genes of the MSigDB: Gene ontology (GO) biological process, cellular component and molecular functions, Reactome pathways, and Hallmark gene sets. The MSigDB hallmark gene sets is a collection of 50 gene sets that provide coherently expressed signatures derived by aggregating many MSigDB gene sets (Molecular Signatures Database v5.2) to represent well-defined biological states or processes (Liberzon et al., 2015). Gene set enrichment scores (NES, p value, FDR and FWER) were provided in the GSEA output format developed by Broad Institute of MIT and Harvard (permutations = 10,000).

Analysis of MCPH1 expression in transcriptomic datasets from the Human BrainSpan Atlas.

To determine the spatiotemporal expression dynamics of modules, we used quantile normalised gene level expression values (log2 transformed) from GSE25219 (Kang et al., 2011). These transcriptome data were generated using Affymetrix Human Exon 1.0 ST array analysis of 16 brain regions comprising the cerebellar cortex, mediodorsal nucleus of the thalamus, striatum, amygdala, hippocampus and 11 areas of the neocortex. The data were generated from 1263 samples collected from 53 clinically unremarkable post-mortem human brains, spanning embryonic development to late adulthood (from 10 weeks of post-conception to 82 years of age, which corresponded to periods 3–15, as previously designated) (Kang et al., 2011). The log2-transformed gene expression data follow a bimodal distribution contributed by low (likely non-functional) and high expressed genes (Hebenstreit et al. 2011). We used the expectation maximisation (EM) algorithm to model gene expression levels as a mixture of normal distributions and identify the underlying distributions of low and high expressed genes. Only the genes, with mean of log2-transformed expression values over the 95 % percentile of distribution of low-expressed genes (here > 5.61) were considered for further analysis (n = 8704). The EM algorithm was implemented using normalMixEM function from the mixtools R package. Spatio-temporal dynamics of MCPH1 across 16 brain regions

and 13 developmental time points were illustrated as a heatmap, as previously described (Pletikos et al., 2014). The resultant heatmap graphs illustrate the changes in expression of *MCPH1* across brain development and cortical regions.

Data statistical analyzes

Statistical analysis was performed with Excel (Microsoft, Richmond, WA) and GraphPad Prism 5.0 (GraphPad Prism Software Inc.). For all cell counts *in vivo*, results were obtained by using at least 3 embryos from at least 2 litters and 2-6 sections per embryo were used for counting. No data was excluded from further analyses. For experiments on NPCs, results were obtained from at least 3 different primary cultures and at least two independent experiments. Sample sizes (n) and statistical methods are indicated in the Figure legends. n is the number of primary cultures or brains used in the experiments. Shapiro-Wilk normality test was used for testing normality of all samples. The two-tailed unpaired Student's *t* test was applied for comparison of two two groups: Ct and cKO brains at P5 and P0, counts of PH3+ and CC3+ cells in 11.5, E12.5, E14.5 and E16.5 Ct and cKO embryonic brains, and for counts of Pax6+, BrdU+ and Tbr2+ cells in E12.5, E14.5 and E16.5 Ct and cKO embryonic brains. The fluorescence ratiometric values of Mito-GEM-GECO1, morphometric measures by electronic microscopy and ROS production data were analyzed using the non-parametric Mann-Whitney U test. Duolink mean values for the experimental groups were calculated and statistically analyzed using the non-parametric Kruskal-Wallis test followed by Dunn's Multiple. Activities of respiratory chain enzymes, of LDH, HKI-IV, IDH and G6PDH, Western blots, cleaved caspase3 in GPGln, PGln, and Gln and FACS cell cycle data were analyzed using one-way ANOVA with Tukey-Kramer Multiple Comparison Tests. In all cases, differences were considered as statistically significant at $p< 0.05$. The meaning of error bars, either SEM or SD, is indicated in the figure legends.

DATA AND CODE AVAILABILITY

The accession number of RNA-seq data generated in this study from WTNPCs and KONPCs is GSE140976.

REFERENCES

Beg, M., Abdullah, N., Thowfeik, F.S., Altorki, N.K., and McGraw, T.E. (2017). Distinct Akt phosphorylation states are required for insulin regulated Glut4 and Glut1-mediated glucose uptake. Elife *6*.

Benit, P., Goncalves, S., Philippe Dassa, E., Briere, J.J., Martin, G., and Rustin, P. (2006). Three spectrophotometric assays for the measurement of the five respiratory chain complexes in minuscule biological samples. Clin Chim Acta *374*, 81-86.

Benit, P., Kahn, A., Chretien, D., Bortoli, S., Huc, L., Schiff, M., Gimenez-Roqueplo, A.P., Favier, J., Gressens, P., Rak, M.*, et al.* (2019). Evolutionarily conserved susceptibility of the mitochondrial respiratory chain to SDHI pesticides and its consequence on the impact of SDHIs on human cultured cells. PLoS One *14*, e0224132.

Betizeau, M., Cortay, V., Patti, D., Pfister, S., Gautier, E., Bellemin-Menard, A., Afanassieff, M., Huissoud, C., Douglas, R.J., Kennedy, H.*, et al.* (2013). Precursor diversity and complexity of lineage relationships in the outer subventricular zone of the primate. Neuron *80*, 442-457.

Betz, C., Stracka, D., Prescianotto-Baschong, C., Frieden, M., Demaurex, N., and Hall, M.N. (2013). Feature Article: mTOR complex 2-Akt signaling at mitochondria-associated endoplasmic reticulum membranes (MAM) regulates mitochondrial physiology. Proc Natl Acad Sci U S A *110*, 12526-12534.

Bultje, R.S., Castaneda-Castellanos, D.R., Jan, L.Y., Jan, Y.N., Kriegstein, A.R., and Shi, S.H. (2009). Mammalian Par3 regulates progenitor cell asymmetric division via notch signaling in the developing neocortex. Neuron *63*, 189-202.

Cardenas, C., Miller, R.A., Smith, I., Bui, T., Molgo, J., Muller, M., Vais, H., Cheung, K.H., Yang, J., Parker, I.*, et al.* (2010). Essential regulation of cell bioenergetics by constitutive InsP3 receptor Ca2+ transfer to mitochondria. Cell *142*, 270-283.

Chen, J.F., Zhang, Y., Wilde, J., Hansen, K.C., Lai, F., and Niswander, L. (2014). Microcephaly disease gene Wdr62 regulates mitotic progression of embryonic neural stem cells and brain size. Nat Commun *5*, 3885.

Chen, H., and Chan, D.C. (2009). Mitochondrial dynamics--fusion, fission, movement, and mitophagy--in neurodegenerative diseases. Hum Mol Genet *18*, R169-176.

Colombo, S.L., Palacios-Callender, M., Frakich, N., Carcamo, S., Kovacs, I., Tudzarova, S., and Moncada, S. (2011). Molecular basis for the differential use of glucose and glutamine in cell proliferation as revealed by synchronized HeLa cells. Proc Natl Acad Sci U S A *108*, 21069-21074.

Dehay, C., Kennedy, H., and Kosik, K.S. (2015). The outer subventricular zone and primate-specific cortical complexification. Neuron *85*, 683-694.

Delahaye-Duriez, A., Srivastava, P., Shkura, K., Langley, S.R., Laaniste, L., Moreno-Moral, A., Danis, B., Mazzuferi, M., Foerch, P., Gazina, E.V.*, et al.* (2016). Rare and common epilepsies converge on a shared gene regulatory network providing opportunities for novel antiepileptic drug discovery. Genome Biol *17*, 245.

Dobin, A., Davis, C.A., Schlesinger, F., Drenkow, J., Zaleski, C., Jha, S., Batut, P., Chaisson, M., and Gingeras, T.R. (2013). STAR: ultrafast universal RNA-seq aligner. Bioinformatics *29*, 15-21.

Duerinckx, S., and Abramowicz, M. (2018). The genetics of congenitally small brains. Semin Cell Dev Biol *76*, 76-85.

El Wakil, A., Francius, C., Wolff, A., Pleau-Varet, J., and Nardelli, J. (2006). The GATA2 transcription factor negatively regulates the proliferation of neuronal progenitors. Development *133*, 2155-2165.

Fish, J.L., Kosodo, Y., Enard, W., Paabo, S., and Huttner, W.B. (2006). Aspm specifically maintains symmetric proliferative divisions of neuroepithelial cells. Proc Natl Acad Sci U S A *103*, 10438-10443.

Flachbartova, Z., and Kovacech, B. (2013). Mortalin - a multipotent chaperone regulating cellular processes ranging from viral infection to neurodegeneration. Acta virologica *57*, 3-15.

Florio, M., Albert, M., Taverna, E., Namba, T., Brandl, H., Lewitus, E., Haffner, C., Sykes, A., Wong, F.K., Peters, J.*, et al.* (2015). Human-specific gene ARHGAP11B promotes basal progenitor amplification and neocortex expansion. Science *347*, 1465-1470.

Florio, M., and Huttner, W.B. (2014). Neural progenitors, neurogenesis and the evolution of the neocortex. Development *141*, 2182-2194.

Frank, C.L., Ge, X., Xie, Z., Zhou, Y., and Tsai, L.H. (2010). Control of activating transcription factor 4 (ATF4) persistence by multisite phosphorylation impacts cell cycle progression and neurogenesis. J Biol Chem *285*, 33324-33337.

Garcez, P.P., Diaz-Alonso, J., Crespo-Enriquez, I., Castro, D., Bell, D., and Guillemot, F. (2015). Cenpj/CPAP regulates progenitor divisions and neuronal migration in the cerebral cortex downstream of Ascl1. Nat Commun *6*, 6474.

Gavvovidis, I., Rost, I., Trimborn, M., Kaiser, F.J., Purps, J., Wiek, C., Hanenberg, H., Neitzel, H., and Schindler, D. (2012). A novel MCPH1 isoform complements the defective chromosome condensation of human MCPH1-deficient cells. PLoS One *7*, e40387.

Godin, J.D., Creppe, C., Laguesse, S., and Nguyen, L. (2016). Emerging Roles for the Unfolded Protein Response in the Developing Nervous System. Trends Neurosci *39*, 394-404.

Gorski, J. A., Talley, T., Qiu, M., Puelles, L., Rubenstein, J. L., Jones, K. R. (2002). Cortical excitatory neurons and glia, but not GABAergic neurons, are produced in the Emx1-expressing lineage. J Neurosci *22*, 6309-14.

Gruber, R., Zhou, Z., Sukchev, M., Joerss, T., Frappart, P.O., and Wang, Z.Q. (2011). MCPH1 regulates the neuroprogenitor division mode by coupling the centrosomal cycle with mitotic entry through the Chk1-Cdc25 pathway. Nature cell biology *13*, 1325-1334.

Gruss, O.J., Wittmann, M., Yokoyama, H., Pepperkok, R., Kufer, T., Sillje, H., Karsenti, E., Mattaj, I.W., and Vernos, I. (2002). Chromosome-induced microtubule assembly mediated by TPX2 is required for spindle formation in HeLa cells. Nature cell biology *4*, 871-879.

Hebenstreit D, Fang M, Gu M, Charoensawan V, van Oudenaarden A, Teichmann SA. RNA sequencing reveals two major classes of gene expression levels in metazoan cells. (2011). Mol Syst Biol *7(497)*, 497.

Hou, X., Liu, Y., Liu, H., Chen, X., Liu, M., Che, H., Guo, F., Wang, C., Zhang, D., Wu, J.*, et al.* (2015). PERK silence inhibits glioma cell growth under low glucose stress by blockage of p-AKT and subsequent HK2's mitochondria translocation. Sci Rep *5*, 9065.

Issa, L., Kraemer, N., Rickert, C.H., Sifringer, M., Ninnemann, O., Stoltenburg-Didinger, G., and Kaindl, A.M. (2013). CDK5RAP2 expression during murine and human brain development correlates with pathology in primary autosomal recessive microcephaly. Cereb Cortex *23*, 2245-2260.

Jackson, A.P., McHale, D.P., Campbell, D.A., Jafri, H., Rashid, Y., Mannan, J., Karbani, G., Corry, P., Levene, M.I., Mueller, R.F.*, et al.* (1998). Primary autosomal recessive microcephaly (MCPH1) maps to chromosome 8p22-pter. Am J Hum Genet *63*, 541-546.

Jayaraman, D., Bae, B.I., and Walsh, C.A. (2018). The Genetics of Primary Microcephaly. Annu Rev Genomics Hum Genet *19*, 177-200.

Kalebic, N., Gilardi, C., Stepien, B., Wilsch-Brauninger, M., Long, K.R., Namba, T., Florio, M., Langen, B., Lombardot, B., Shevchenko, A.*, et al.* (2019). Neocortical Expansion Due to Increased Proliferation of Basal Progenitors Is Linked to Changes in Their Morphology. Cell Stem Cell *24*, 535-550 e539.

Kang, H.J., Kawasawa, Y.I., Cheng, F., Zhu, Y., Xu, X., Li, M., Sousa, A.M., Pletikos, M., Meyer, K.A., Sedmak, G.*, et al.* (2011). Spatio-temporal transcriptome of the human brain. Nature *478*, 483-489.

Laguesse, S., Creppe, C., Nedialkova, D.D., Prevot, P.P., Borgs, L., Huysseune, S., Franco, B., Duysens, G., Krusy, N., Lee, G.*, et al.* (2015). A Dynamic Unfolded Protein Response Contributes to the Control of Cortical Neurogenesis. Dev Cell *35*, 553-567.

Lange, C., Turrero Garcia, M., Decimo, I., Bifari, F., Eelen, G., Quaegebeur, A., Boon, R., Zhao, H., Boeckx, B., Chang, J.*, et al.* (2016). Relief of hypoxia by angiogenesis promotes neural stem cell differentiation by targeting glycolysis. EMBO J *35*, 924-941.

Lassot, I., Segeral, E., Berlioz-Torrent, C., Durand, H., Groussin, L., Hai, T., Benarous, R., and Margottin-Goguet, F. (2001). ATF4 degradation relies on a phosphorylation-dependent interaction with the SCF(betaTrCP) ubiquitin ligase. Mol Cell Biol *21*, 2192-2202.

Liang, Y., Gao, H., Lin, S.Y., Peng, G., Huang, X., Zhang, P., Goss, J.A., Brunicardi, F.C., Multani, A.S., Chang, S.*, et al.* (2010). BRIT1/MCPH1 is essential for mitotic and meiotic recombination DNA repair and maintaining genomic stability in mice. PLoS genetics *6*, e1000826.

Liberzon, A., Birger, C., Thorvaldsdottir, H., Ghandi, M., Mesirov, J.P., and Tamayo, P. (2015). The Molecular Signatures Database (MSigDB) hallmark gene set collection. Cell Syst *1*, 417-425.

Liu, X., Zong, W., Li, T., Wang, Y., Xu, X., Zhou, Z.W., and Wang, Z.Q. (2017). The E3 ubiquitin ligase APC/C(C)(dh1) degrades MCPH1 after MCPH1-betaTrCP2-Cdc25A-mediated mitotic entry to ensure neurogenesis. EMBO J.

Lui, J.H., Hansen, D.V., and Kriegstein, A.R. (2011). Development and evolution of the human neocortex. Cell *146*, 18-36.

Martinez-Martinez, M.A., De Juan Romero, C., Fernandez, V., Cardenas, A., Gotz, M., and Borrell, V. (2016). A restricted period for formation of outer subventricular zone defined by Cdh1 and Trnp1 levels. Nat Commun *7*, 11812.

Mendez-Lucas, A., Hyrossova, P., Novellasdemunt, L., Vinals, F., and Perales, J.C. (2014). Mitochondrial phosphoenolpyruvate carboxykinase (PEPCK-M) is a pro-survival, endoplasmic reticulum (ER) stress response gene involved in tumor cell adaptation to nutrient availability. J Biol Chem *289*, 22090-22102.

Naro, C., Jolly, A., Di Persio, S., Bielli, P., Setterblad, N., Alberdi, A.J., Vicini, E., Geremia, R., De la Grange, P., and Sette, C. (2017). An Orchestrated Intron Retention Program in Meiosis Controls Timely Usage of Transcripts during Germ Cell Differentiation. Dev Cell *41*, 82-93 e84.

Noli, L., Capalbo, A., Ogilvie, C., Khalaf, Y., and Ilic, D. (2015). Discordant Growth of Monozygotic Twins Starts at the Blastocyst Stage: A Case Study. Stem Cell Reports *5*, 946-953.

Nowakowski, T.J., Bhaduri, A., Pollen, A.A., Alvarado, B., Mostajo-Radji, M.A., Di Lullo, E., Haeussler, M., Sandoval-Espinosa, C., Liu, S.J., Velmeshev, D.*, et al.* (2017). Spatiotemporal gene expression trajectories reveal developmental hierarchies of the human cortex. Science *358*, 1318-1323.

Olalla, L., Gutierrez, A., Campos, J.A., Khan, Z.U., Alonso, F.J., Segura, J.A., Marquez, J., and Aledo, J.C. (2002). Nuclear localization of L-type glutaminase in mammalian brain. J Biol Chem *277*, 38939-38944.

Park, D., Xiang, A. P., Zhang, L., Mao, F. F., Walton, N. M., Choi, S. S. and Lahn, B. T. (2009). The radial glia antibody RC2 recognizes a protein encoded by Nestin. Biochem Biophys Res Commun., *382*, 588-92.

Peng, G., Yim, E.K., Dai, H., Jackson, A.P., Burgt, I., Pan, M.R., Hu, R., Li, K., and Lin, S.Y. (2009). BRIT1/MCPH1 links chromatin remodelling to DNA damage response. Nature cell biology *11*, 865-872.

Pletikos, M., Sousa, A.M., Sedmak, G., Meyer, K.A., Zhu, Y., Cheng, F., Li, M., Kawasawa, Y.I., and Sestan, N. (2014). Temporal specification and bilaterality of human neocortical topographic gene expression. Neuron *81*, 321-332.

Pulvers, J.N., Journiac, N., Arai, Y., and Nardelli, J. (2015). MCPH1: a window into brain development and evolution. Frontiers in cellular neuroscience *9*, 92.

Roberts, D.J., Tan-Sah, V.P., Smith, J.M., and Miyamoto, S. (2013). Akt phosphorylates HK-II at Thr-473 and increases mitochondrial HK-II association to protect cardiomyocytes. J Biol Chem *288*, 23798-23806.

Rodriguez, C.I., Buchholz, F., Galloway, J., Sequerra, R., Kasper, J., Ayala, R., Stewart, A.F., and Dymecki, S.M. (2000). High-efficiency deleter mice show that FLPe is an alternative to Cre-loxP. Nat Genet *25*, 139-140.

Rustin, P., Chretien, D., Bourgeron, T., Gerard, B., Rotig, A., Saudubray, J.M., and Munnich, A. (1994). Biochemical and molecular investigations in respiratory chain deficiencies. Clin Chim Acta *228*, 35-51.

Schindelin, J., Arganda-Carreras, I., Frise, E., Kaynig, V., Longair, M., Pietzsch, T., Preibisch, S., Rueden, C., Saalfeld, S., Schmid, B.*, et al.* (2012). Fiji: an open-source platform for biological-image analysis. Nat Methods *9*, 676-682.

Schneider, C.A., Rasband, W.S., and Eliceiri, K.W. (2012). NIH Image to ImageJ: 25 years of image analysis. Nat Methods *9*, 671-675.

Shashidharan, P., Michaelidis, T.M., Robakis, N.K., Kresovali, A., Papamatheakis, J., and Plaitakis, A. (1994). Novel human glutamate dehydrogenase expressed in neural and testicular tissues and encoded by an X-linked intronless gene. J Biol Chem *269*, 16971-16976.

Subramanian, A., Tamayo, P., Mootha, V.K., Mukherjee, S., Ebert, B.L., Gillette, M.A., Paulovich, A., Pomeroy, S.L., Golub, T.R., Lander, E.S.*, et al.* (2005). Gene set enrichment analysis: a

knowledge-based approach for interpreting genome-wide expression profiles. Proc Natl Acad Sci U S A *102*, 15545-15550.

Szabadkai, G., Bianchi, K., Varnai, P., De Stefani, D., Wieckowski, M.R., Cavagna, D., Nagy, A.I., Balla, T., and Rizzuto, R. (2006). Chaperone-mediated coupling of endoplasmic reticulum and mitochondrial Ca2+ channels. J Cell Biol *175*, 901-911.

Terada, Y., Tatsuka, M., Suzuki, F., Yasuda, Y., Fujita, S., and Otsu, M. (1998). AIM-1: a mammalian midbody-associated protein required for cytokinesis. EMBO J *17*, 667-676.

Vincent, E.E., Sergushichev, A., Griss, T., Gingras, M.C., Samborska, B., Ntimbane, T., Coelho, P.P., Blagih, J., Raissi, T.C., Choiniere, L.*, et al.* (2015). Mitochondrial Phosphoenolpyruvate Carboxykinase Regulates Metabolic Adaptation and Enables Glucose-Independent Tumor Growth. Mol Cell *60*, 195-207.

Wagenfuhr, L., Meyer, A.K., Braunschweig, L., Marrone, L., and Storch, A. (2015). Brain oxygen tension controls the expansion of outer subventricular zone-like basal progenitors in the developing mouse brain. Development *142*, 2904-2915.

Yang, Y.T., Wang, C.L., and Van Aelst, L. (2012). DOCK7 interacts with TACC3 to regulate interkinetic nuclear migration and cortical neurogenesis. Nat Neurosci *15*, 1201-1210.

Zheng, X., Boyer, L., Jin, M., Mertens, J., Kim, Y., Ma, L., Ma, L., Hamm, M., Gage, F.H., and Hunter, T. (2016). Metabolic reprogramming during neuronal differentiation from aerobic glycolysis to neuronal oxidative phosphorylation. Elife *5*.

Zhao, Y., Araki, S., Wu, J., Teramoto, T., Chang, Y. F., Nakano, M., Abdelfattah, A. S., Fujiwara, M., Ishihara, T., Nagai, T., Campbell, R. E. (2011). An expanded palette of genetically encoded Ca(2)(+)

1 indicators. Science *333*, 1888-92

2
3

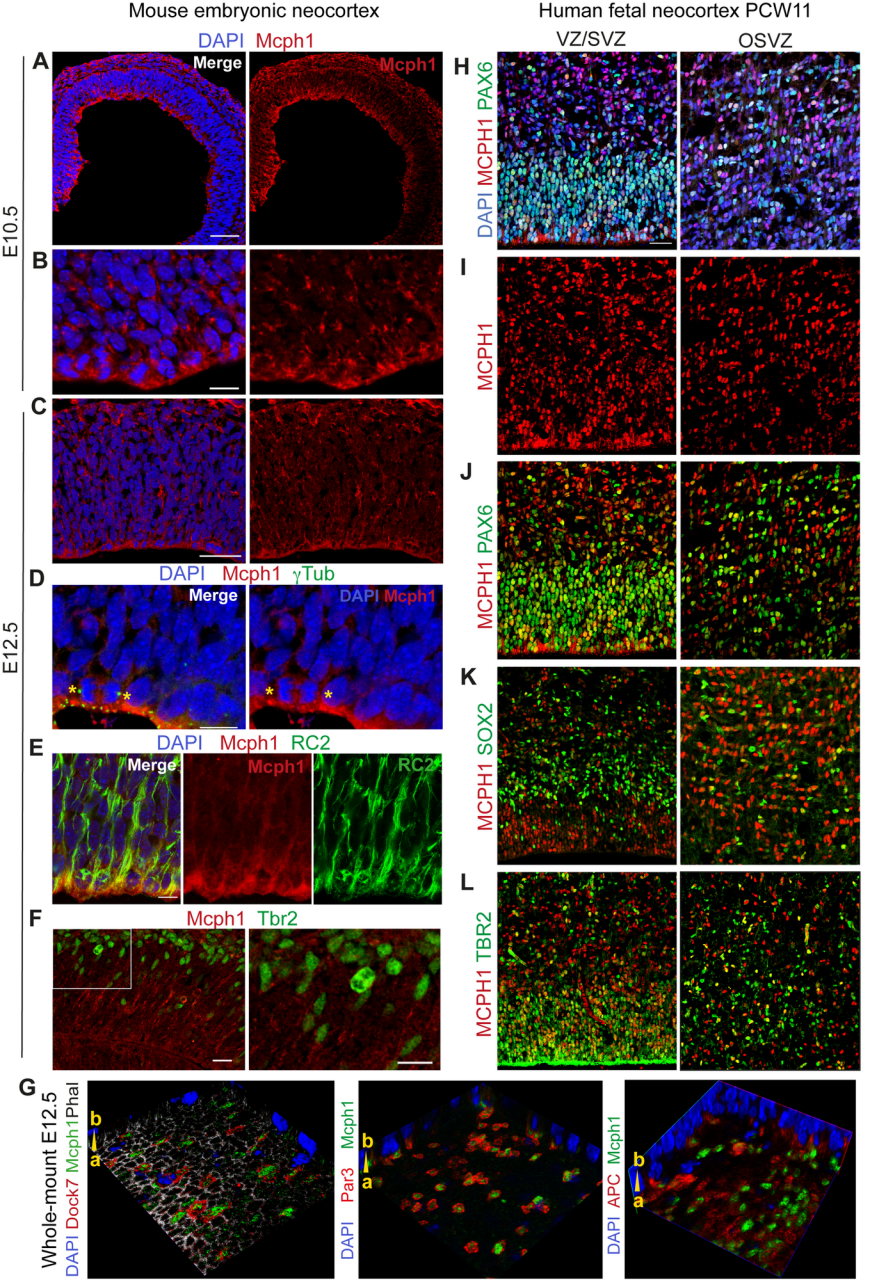
Mouse embryonic neocortex
Human fetal neocortex PCW11
VZ/SVZ
OSVZ
E10.5
E12.5
A
B
C
D
E
F
G
H
I
J
K
L
DAPI Mcph1
Merge
Mcph1
DAPI Mcph1 γTub
DAPI Mcph1 RC2
RC2
Mcph1 Tbr2
DAPI MCPH1 PAX6
MCPH1
MCPH1 PAX6
MCPH1 SOX2
MCPH1 TBR2
Whole-mount E12.5
DAPI Dock7 Mcph1 Phal
DAPI Par3 Mcph1
DAPI APC Mcph1
b
a

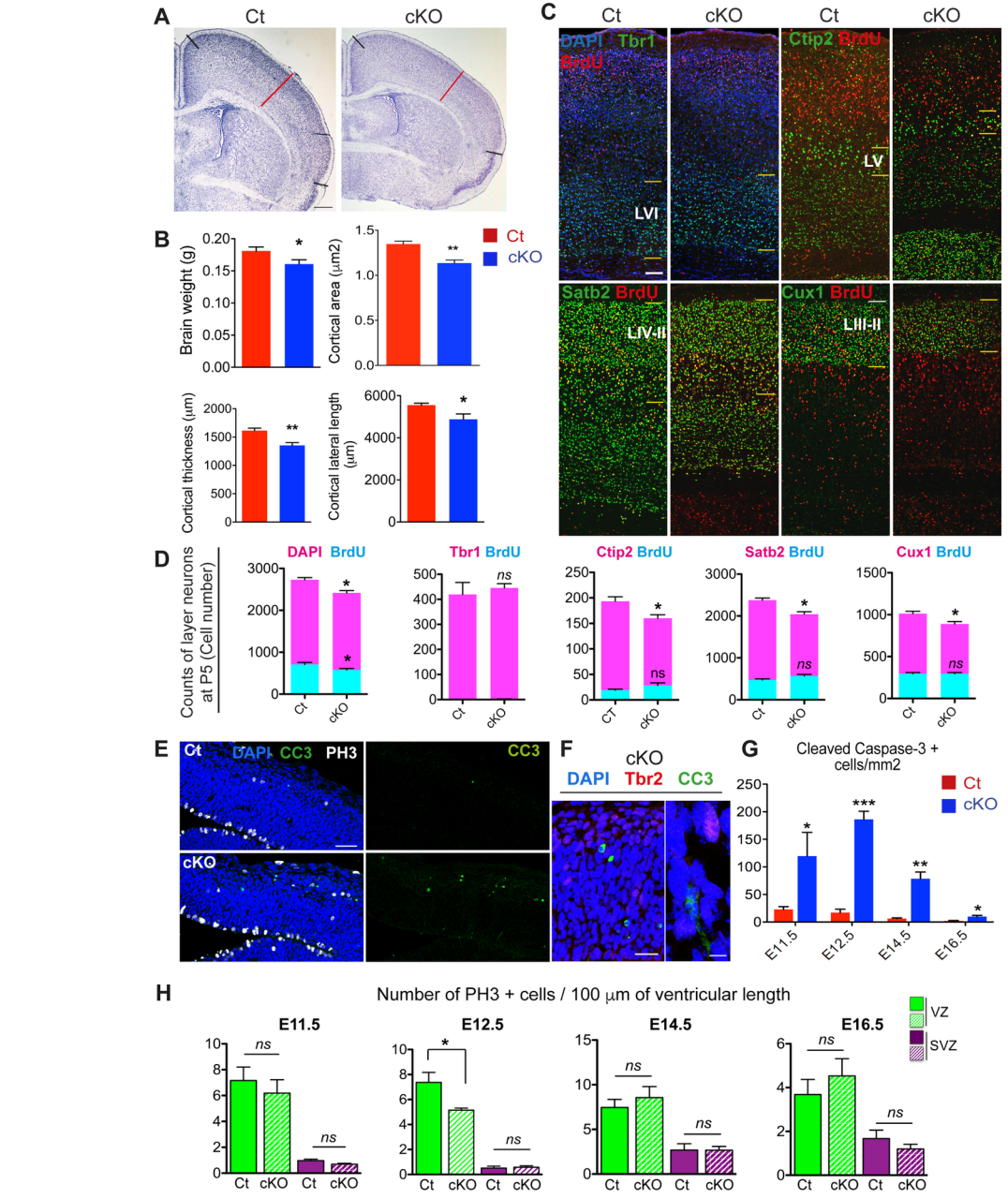
A
Ct
cKO
B
Brain weight (g)
Cortical area (μm2)
Cortical thickness (μm)
Cortical lateral length (μm)
Ct
cKO
C
DAPI Tbr1 BrdU
Ctip2 BrdU
Satb2 BrdU
Cux1 BrdU
LV
LVI
LIV-II
LIII-II
D
Counts of layer neurons at P5 (Cell number)
DAPI BrdU
Tbr1 BrdU
Ctip2 BrdU
Satb2 BrdU
Cux1 BrdU
ns
E
DAPI CC3 PH3
CC3
F
cKO
DAPI Tbr2 CC3
G
Cleaved Caspase-3 + cells/mm2
E11.5
E12.5
E14.5
E16.5
H
Number of PH3 + cells / 100 μm of ventricular length
VZ
SVZ

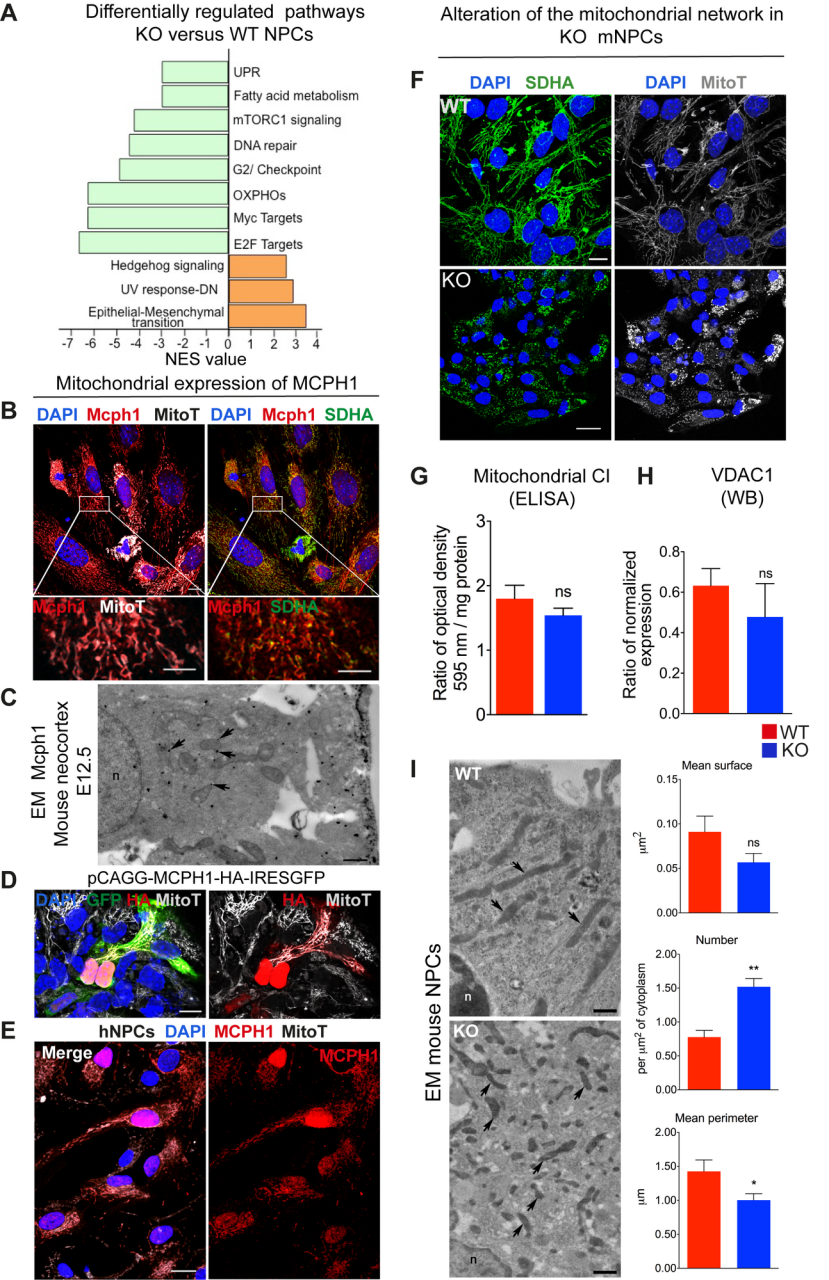
A
Differentially regulated pathways
KO versus WT NPCs
UPR
Fatty acid metabolism
mTORC1 signaling
DNA repair
G2/ Checkpoint
OXPHOs
Myc Targets
E2F Targets
Hedgehog signaling
UV response-DN
Epithelial-Mesenchymal transition
-7 -6 -5 -4 -3 -2 -1 0 1 2 3 4
NES value
Mitochondrial expression of MCPH1
B
DAPI Mcph1 MitoT
DAPI Mcph1 SDHA
Mcph1 MitoT
Mcph1 SDHA
C
EM Mcph1
Mouse neocortex
E12.5
n
D
pCAGG-MCPH1-HA-IRESGFP
DAPI GFP HA MitoT
HA MitoT
E
hNPCs DAPI MCPH1 MitoT
Merge
MCPH1
Alteration of the mitochondrial network in
KO mNPCs
F
DAPI SDHA
DAPI MitoT
WT
KO
G
Mitochondrial CI
(ELISA)
Ratio of optical density
595 nm / mg protein
ns
H
VDAC1
(WB)
Ratio of normalized
expression
ns
WT
KO
I
EM mouse NPCs
WT
KO
n
Mean surface
µm2
ns
Number
per µm2 of cytoplasm
**
Mean perimeter
µm
*

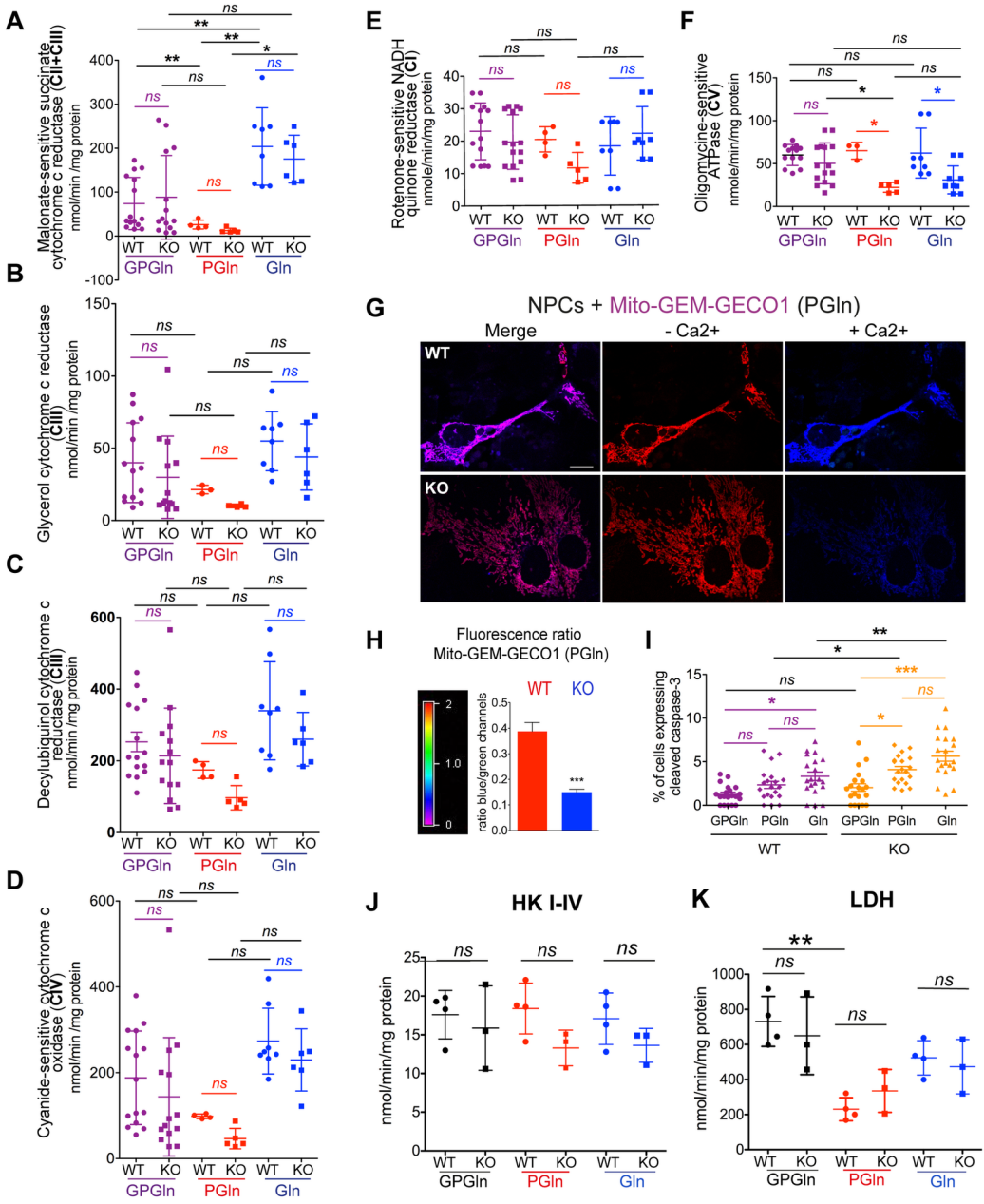
A
Malonate-sensitive succinate cytochrome c reductase (CII+CIII)
nmol/min /mg protein
B
Glycerol cytochrome c reductase (CIII)
nmol/min /mg protein
C
Decylubiquinol cytochrome c reductase (CIII)
nmol/min /mg protein
D
Cyanide-sensitive cytochrome c oxidase (CIV)
nmol/min /mg protein
E
Rotenone-sensitive NADH quinone reductase (CI)
nmole/min/mg protein
F
Oligomycine-sensitive ATPase (CV)
nmole/min/mg protein
WT KO WT KO WT KO
GPGln PGln Gln
ns
G
NPCs + Mito-GEM-GECO1 (PGln)
Merge
- Ca2+
+ Ca2+
WT
KO
H
Fluorescence ratio
Mito-GEM-GECO1 (PGln)
ratio blue/green channels
WT KO
I
% of cells expressing cleaved caspase-3
GPGln PGln Gln GPGln PGln Gln
WT KO
J
HK I-IV
nmol/min/mg protein
K
LDH
nmol/min/mg protein

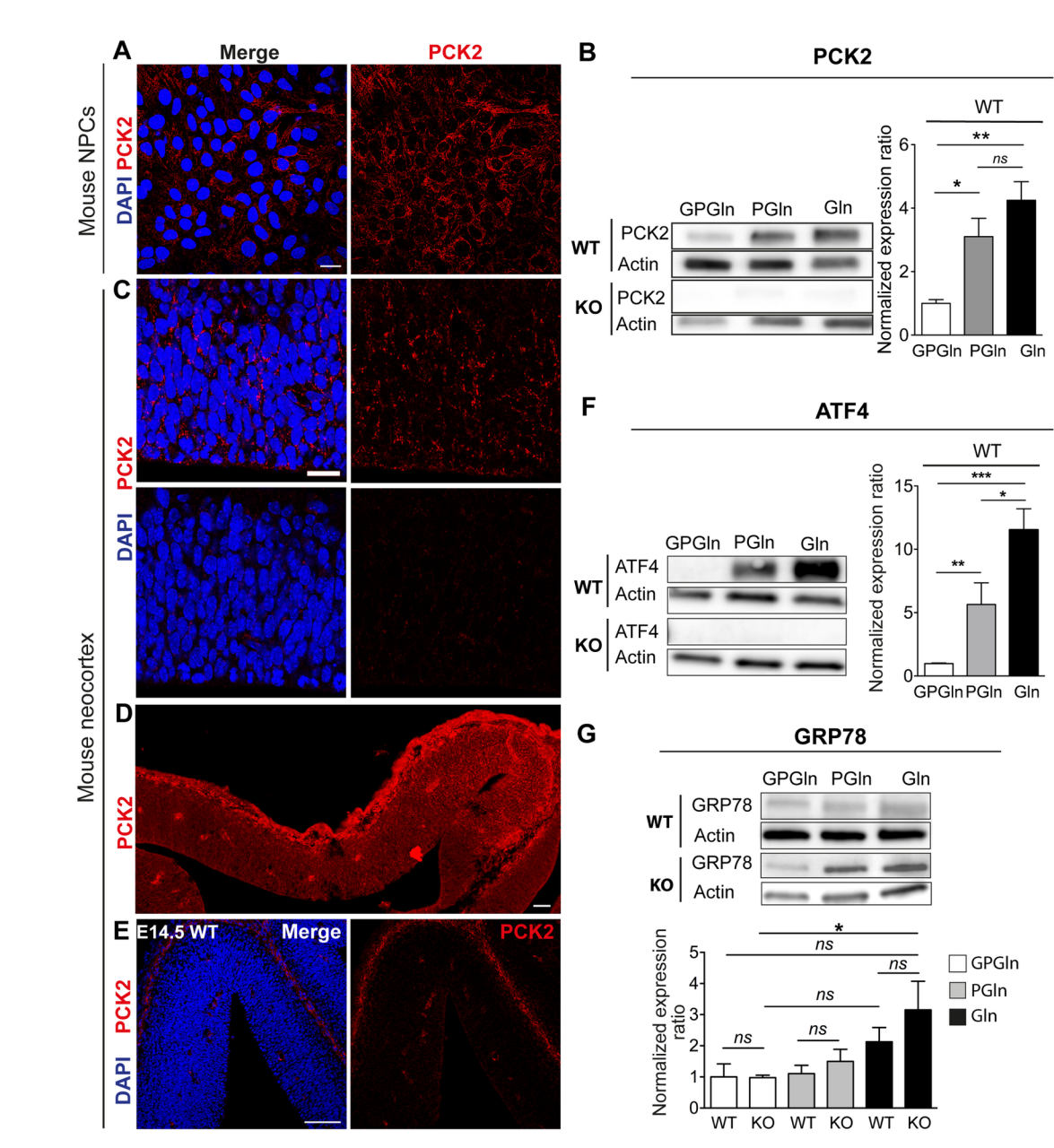
A
Merge
PCK2
Mouse NPCs
DAPI PCK2
B
PCK2
GPGln PGln Gln
WT
PCK2
Actin
KO
PCK2
Actin
WT
Normalized expression ratio
GPGln PGln Gln
C
PCK2
DAPI
Mouse neocortex
D
PCK2
E
E14.5 WT
Merge
PCK2
DAPI
F
ATF4
GPGln PGln Gln
WT
ATF4
Actin
KO
ATF4
Actin
WT
Normalized expression ratio
GPGln PGln Gln
G
GRP78
GPGln PGln Gln
WT
GRP78
Actin
KO
GRP78
Actin
Normalized expression ratio
GPGln
PGln
Gln
WT KO WT KO WT KO

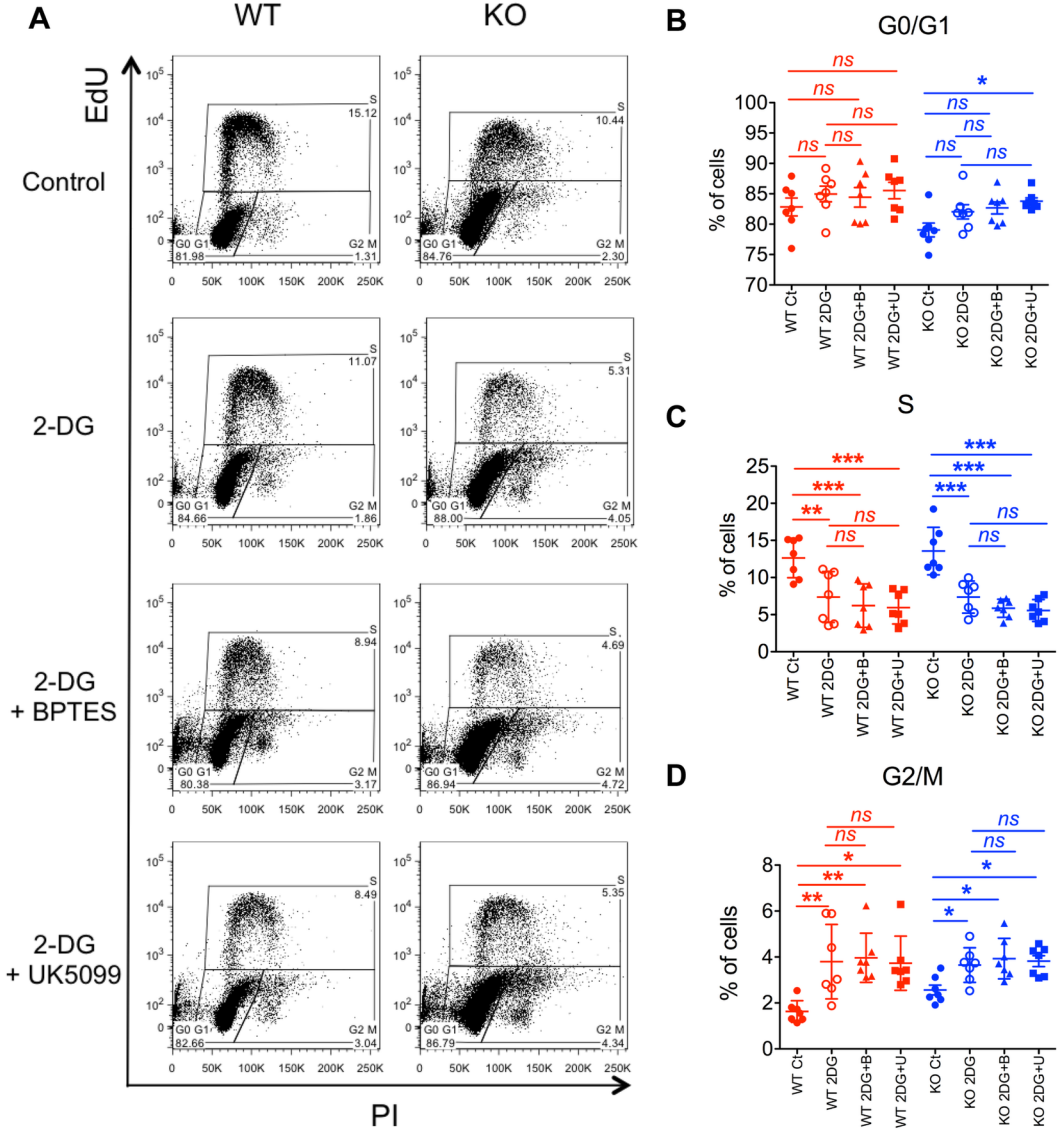
A
WT
KO
EdU
PI
Control
2-DG
2-DG + BPTES
2-DG + UK5099
S
G0 G1
G2 M
15.12
1.31
81.98
10.44
2.30
84.76
11.07
1.86
84.66
5.31
4.05
88.00
8.94
3.17
80.38
4.69
4.72
86.94
8.49
3.04
82.66
5.35
4.34
86.79
0 50K 100K 150K 200K 250K
B
G0/G1
% of cells
ns
*
C
S
***
**
D
G2/M
WT Ct
WT 2DG
WT 2DG+B
WT 2DG+U
KO Ct
KO 2DG
KO 2DG+B
KO 2DG+U

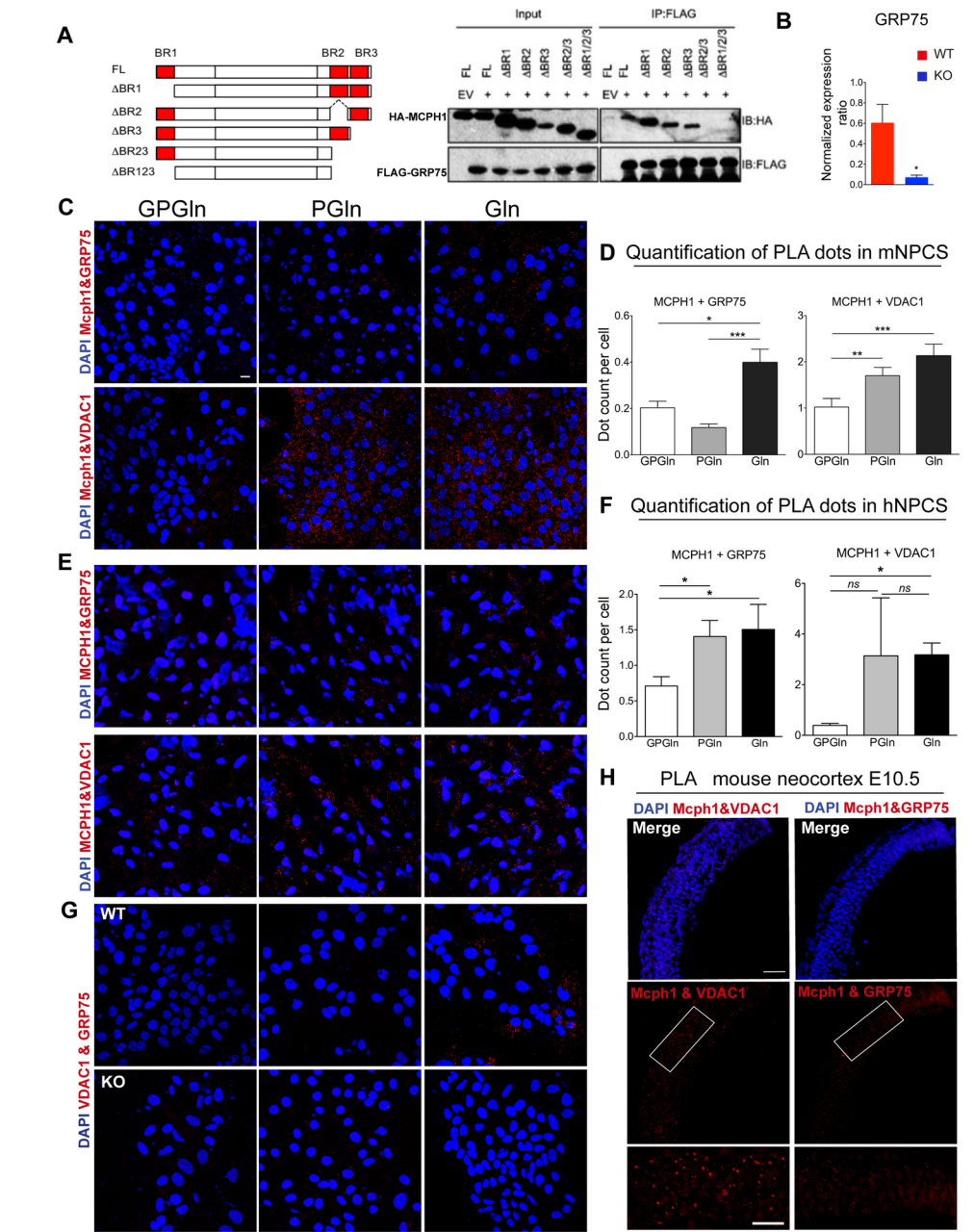
A
BR1
BR2
BR3
FL
ΔBR1
ΔBR2
ΔBR3
ΔBR23
ΔBR123
Input
IP:FLAG
FL
EV
ΔBR1
ΔBR2
ΔBR3
ΔBR2/3
ΔBR1/2/3
HA-MCPH1
FLAG-GRP75
IB:HA
IB:FLAG
B
GRP75
WT
KO
Normalized expression ratio
C
GPGln
PGln
Gln
DAPI Mcph1&GRP75
DAPI Mcph1&VDAC1
D
Quantification of PLA dots in mNPCS
MCPH1 + GRP75
MCPH1 + VDAC1
Dot count per cell
GPGln
PGln
Gln
E
DAPI MCPH1&GRP75
DAPI MCPH1&VDAC1
F
Quantification of PLA dots in hNPCS
MCPH1 + GRP75
MCPH1 + VDAC1
ns
G
WT
KO
DAPI VDAC1 & GRP75
H
PLA mouse neocortex E10.5
DAPI Mcph1&VDAC1
DAPI Mcph1&GRP75
Merge
Mcph1 & VDAC1
Mcph1 & GRP75

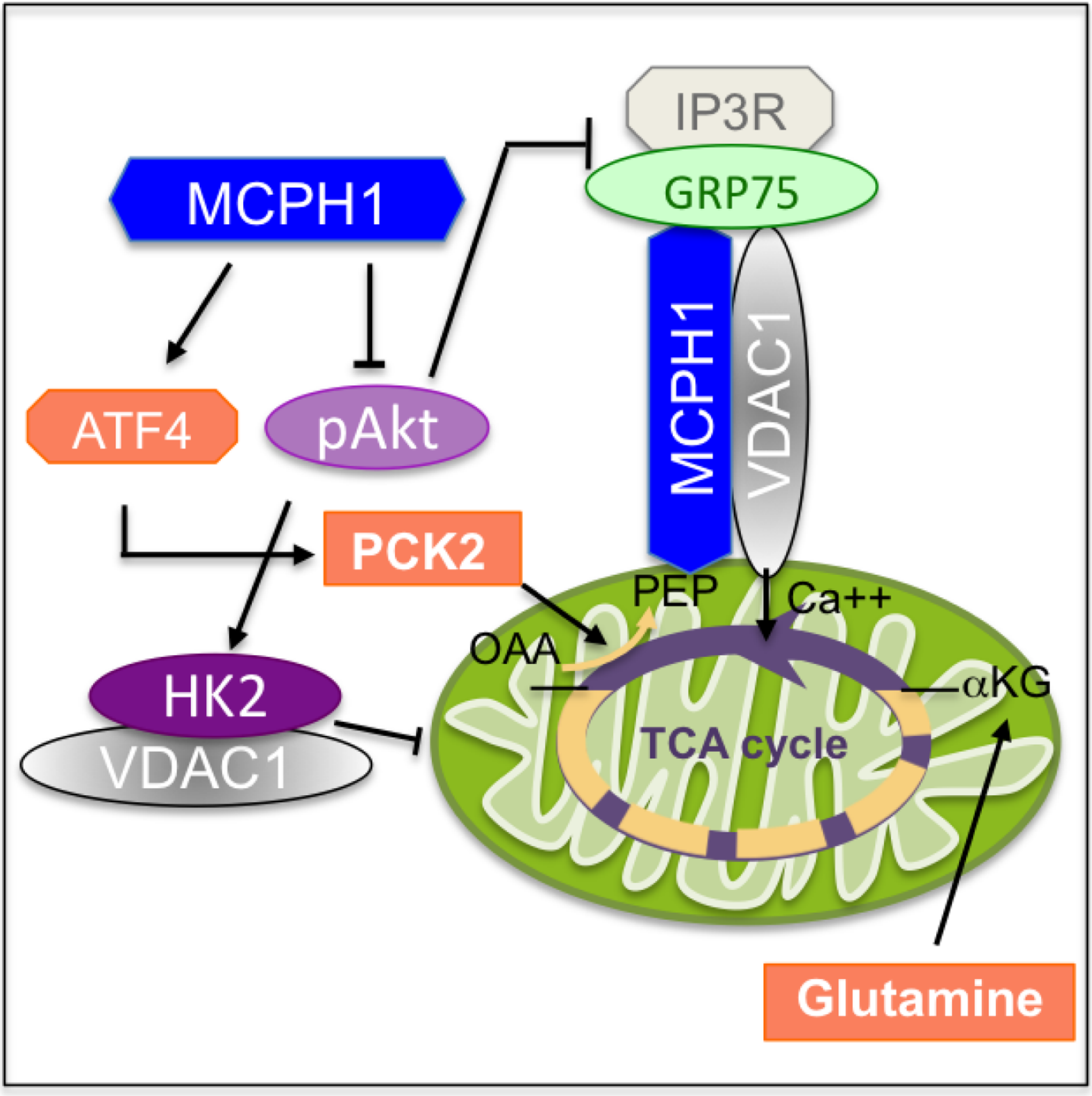
IP3R
GRP75
MCPH1
MCPH1
VDAC1
ATF4
pAkt
PCK2
PEP
Ca++
OAA
αKG
HK2
VDAC1
TCA cycle
Glutamine